Astronomy & Astrophysics manuscript no. Rosetta_photometry_referee_v2 ©ESO 2015
June 12, 2015

Photometric properties of comet 67P/Churyumov-Gerasimenko from VIRTIS-M onboard Rosetta

M. Ciarniello[1], F. Capaccioni[1], G. Filacchione[1], A. Raponi[1], F. Tosi[1], M. C. De Sanctis[1], M. T. Capria[1], S. Erard[2], D. Bockelee-Morvan[2], C. Leyrat[2], G. Arnold[3], A. Barucci[2], P. Beck[4], G. Bellucci[1], S. Fornasier[2], A. Longobardo[1], S. Mottola[3], E. Palomba[1], E. Quirico[4], and B. Schmitt[4]

(Affiliations can be found after the references)

June 12, 2015

ABSTRACT

Aims. We investigate the nucleus photometric properties of the comet 67P/Churyumov-Gerasimenko as observed by the the Visible and Infrared Thermal Imaging Spectrometer (VIRTIS) onboard the Rosetta spacecraft. Both full-disk and disk-resolved images of the comet have been analyzed, deriving light and phase curves as well as a photometric reduction of the measured I/F to single scattering albedo in the 0.4-3.5 μm range.

Methods. Hyper-spectral cubes from VIRTIS were calibrated and corrected for instrumental artifacts. We computed integrated fluxes from full-disk acquisitions in order to derive nucleus light curves and phase curves at low phase angles ($1.2^\circ < \alpha < 14.9^\circ$). Disk-resolved observations in the phase angle range $27.2^\circ < \alpha < 111.5^\circ$ have been reduced to single scattering albedo (SSA) by means of a simplified Hapke's model, deriving average spectrophotometric properties of the surface and producing SSA maps at different wavelenghts. Spectral phase reddening in the visible (VIS) and infrared (IR) ranges has been measured. Finally, full-disk and disk-resolved data have been used together to derive a phase curve of the nucleus in the $1.2^\circ < \alpha < 111.5^\circ$ range.

Results. We measure an asymmetric double-peaked light curve, due to the elongated shape of the nucleus. The average SSA albedo shows a reddish spectrum with an important absorption feature centered at 3.2 μm while the surface exhibits a backscattering behavior. The derived geometric albedo is $A_{geo} = 0.062 \pm 0.002$ at 0.55 μm, indicating a very dark surafce. Phase reddening is significant both in the VIS and IR ranges and we report spectral slopes of $20\%/k$Å and $3.3\%/k$Å respectively, after the application of the photometric reduction. SSA maps indicate that Hapi and Imothep regions are the brightest in the VIS, with the former showing a bluer spectrum with

respect to the rest of the surface. The phase curve of the nucleus shows an important opposition effect, with $\beta = 0.082 \pm 0.015$ for $\alpha < 15°$.

Key words. methods: data analysis – techniques: photometric – techniques: spectroscopic – comets: individual: 67P/Churyumov-Gerasimenko

1. Introduction and rationale

After a cruise phase of more than ten years the Rosetta spacecraft entered orbit around comet 67P/Churyumov-Gerasimenko (CG) on 6 August 2014. From this date the spacecraft began to escort the comet and will follow it till the end of the nominal mission (December 2015). This allowed very accurate nucleus imaging making 67P/CG the sixth comet to be directly observed from a spacecraft after 1P/Halley , 9P/Tempel 1, 19P/Borrelly, 81P/Wild 2 and 103P/Hartley 2 . The Rosetta orbiter carries eleven instruments and among these, VIRTIS, the Visible and Infrared Thermal Imaging Spectrometer (Coradini et al. 2007). This experiment is composed of two sensor heads, -M (Mapper) and -H (High resolution). The -H sensor is a high resolution punctual spectrometer mainly devoted to the study of the coma properties in the 1.88-5.03 μm, while -M produces hyperspectral images of the target in the 0.2-5.1 μm range with an angular resolution of 250 μrad $\times$ 250 μrad. Data from VIRTIS-M are crucial to assess nucleus spectrophotometric properties: on global scale with disk-integrated observations and, thanks to its imaging capabilities, at larger spatial resolutions with disk-resolved measurements. The latter case is of paramount importance in order to map compositional variability on the surface and possibly link it to sources of activity.
This work focuses on VIRTIS-M data acquired from July 2014 up to February 2015. The analysis we performed is divided into two main subjects: full-disk photometry (sec. 2) and disk-resolved photometry (sec. 3). In sec. 2, we discuss rotational curves (sec. 2.1), full-disk phase curves (sec. 2.2), color ratios (sec. 2.3) and the derivation of the geometric albedo (sec. 2.4). In sec. 3, taking advantage of the large dataset acquired by VIRTIS-M we calculate a photometric reduction by means of a Hapke simplified model thus assessing the spectrophotometric properties of the surface. Also a zonal photometric reduction has been derived for four macro-regions, in order to better investigate compositional and morphological differences on the nucleus (sec. 3.6). In sec. 4 the full-disk and the disk-resolved dataset are used together to derive a complete phase curve of the comet. Finally a comparison to photometric properties of other comets is shown in sec. 5 and in sec. 6 a summary of the main findings is reported as well as a discussion of future developments of this work with new observations in the coming months.

2. Full-disk photometry

In this section we analyze the photometric properties of 67P/Churyumov-Gerasimenko as observed by VIRTIS instrument during the approach phase to the comet (MTP005 phase). Acquisitions

have been taken on July 2014 when the comet was at an heliocentric distance of approximately 3.7 AU and in this period the target-spacecraft distance decreased from 13000 km down to 1800 km. As a consequence the pixel dimension at surface decreased from 3.2 km to 450 m and the portion of VIRTIS field of view (FOV) occupied by the comet varied from a couple of pixels up to few tens. The whole dataset, here, as in the the following sections, has been corrected for residual instrumental artifact following the method described in Raponi (2015). Given the low spatial resolution of this acquisitions and the relative low amount of pixels available for the analysis, a disk-resolved photometric study was not feasible thus justifying a disk-integrated approach. To this aim the signal of the whole VIRTIS FOV has been summed for each hyper-spectral cube at each wavelength producing a full-disk spectral reflectance. Coma contribution to the total signal can be considered as negligible given the low activity of the comet, due to the large heliocentric distance at that time. However, the average signal measured from background pixels is subtracted, thus removing residual dark current contributions and minimizing light scattered from the coma. **Background pixels have been selected as theclosest to the comet disk image in the FOV, where signal from nucleus could not be recognized.** Each acquisition is characterized by a value of the solar phase angle ($1.2° < \alpha < 14.9°$) as well as of the rotational phase. This allows us to produce both light curves and phase curves of the comet as shown below in sec. 2.1 and 2.2.

2.1. Light curves

In fig. 1 we report the light curves of the comet CG as derived from VIRTIS MTP005 observations. Since VIRTIS signal is calibrated into standard radiance units $W/m^2/\mu m/sr$, in order to compare our result with previous measurements by Mottola et al. (2014), the derived flux ($F_{CG,R}$, $[W/m^2]$) has been converted into reduced planetary magnitudes in the R band ($R(1,1,g)$) **after convolution with the Kron-Cousins R** filter band pass of (Bessell 1986), by means of the following relations (Lagerkvist & Magnusson 1990):

$$\begin{aligned} F_{CG,R} &= \Sigma_i I_{R,i} \delta\epsilon \\ m_R &= m_{\odot,R} - 2.5 \log \frac{F_{CG,R}}{F_{\odot,R}} \\ R(1,1,\alpha) &= m_R - 5 \log r \cdot \Delta \end{aligned} \tag{1}$$

where $I_{R,i}$ is the pixel radiance, $\delta\epsilon$ the instrumental instantaneous FOV (IFOV), m_R the comet relative magnitude, $m_{\odot,R}$ the Sun relative magnitude, $F_{\odot,R}$ the Sun flux at the comet heliocentric distance r and Δ the spacecraft-comet distance. Both r and Δ are expressed in astronomical units while the subscript R indicates that values are referred to the R band. Errors bars are derived with the VIRTIS Signal to Noise Ratio simulator described in Raponi (2015). In fig. 1 points are grouped according to their phase angle α. Because of the elongated irregular shape of CG these curves are double peaked with the primary maximum larger than the secondary. Moreover they are shifted

towards lower magnitudes for decreasing phase angle, since a larger portion of the comet is both visible and illuminated and because of the opposition effect (OE) surge (Hapke et al. 1998). For comparison we report the light curve derived by the OSIRIS camera onboard Rosetta (Mottola et al. 2014) at $\alpha = 32.6°$, which gives evidence of good agreement between the results of the two instruments.

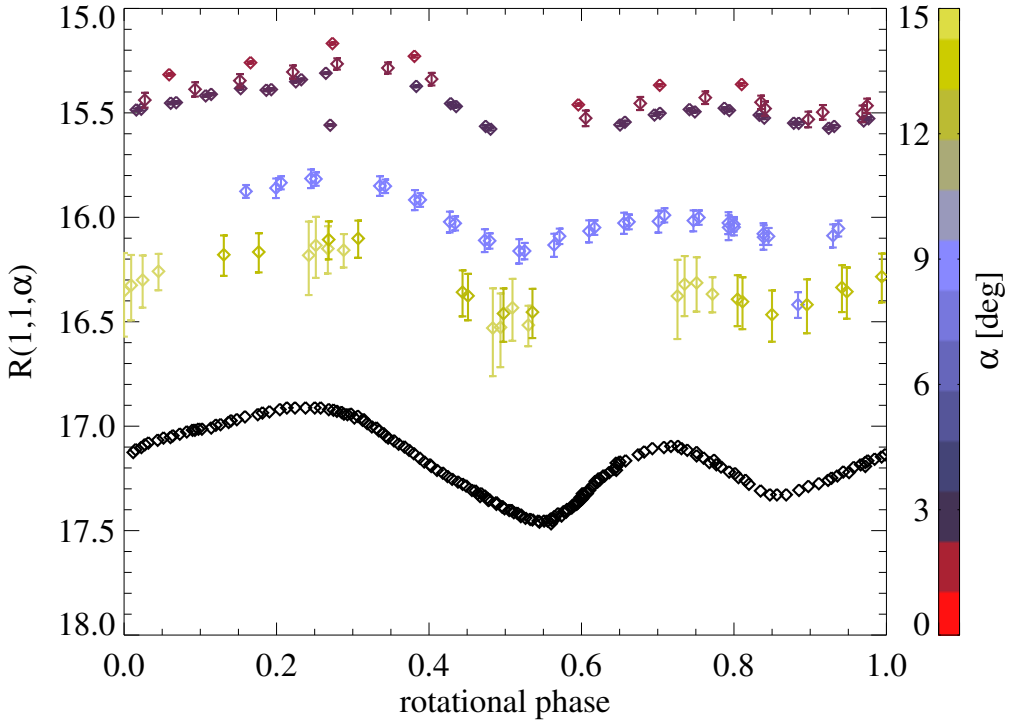

Fig. 1: Light curve in the R band. Black diamonds are from light curve as measured by OSIRIS camera onboard Rosetta (Mottola et al. 2014), arbitrarily shifted to match the rotational phase of VIRTIS observations. We assumed a comet rotational period of 12.4043 ± 0.0007 h (Sierks et al. 2015). Rotational phase is set to 0 at the time of the first VIRTIS acquisition T_0 = 56850.0 MJD (Modified Julian Date). Color bar provides the phase angle scale in degrees for VIRTIS observations.

2.2. Low phase integrated phase curves

From the same dataset described in sec. 2.2 the phase curve of the comet has been derived, as shown in fig. 2. Four different wavelengths, 0.55 μm, 0.80 μm, 1 μm and 2 μm are shown. Data with similar phase angles but acquired at different rotational phases have been averaged into 1° phase angle bins. The phase curves have been normalized at the lowest phase angle $\alpha = 1°$. The shape of the phase curve clearly displays a well developed opposition effect (OE) below 10 °. No strong dependence on wavelength is observed, thus indicating that Shadow Hiding OE is the dominant mechanism (Hapke 1993), with Coherent Backscattering OE possibly relevant only for phase angles lower than 1° (Hapke 2002; Kaydash et al. 2013). A rigorous analytic description of the OE in the case of full-disk observations can be applied only in the case of a spherical body (Hapke 1993, 2012), which is

not the case of the comet CG. For this reason we decided to postpone a full characterization of OE parameters to a future work, when low phase angle disk-resolved observations will be available.

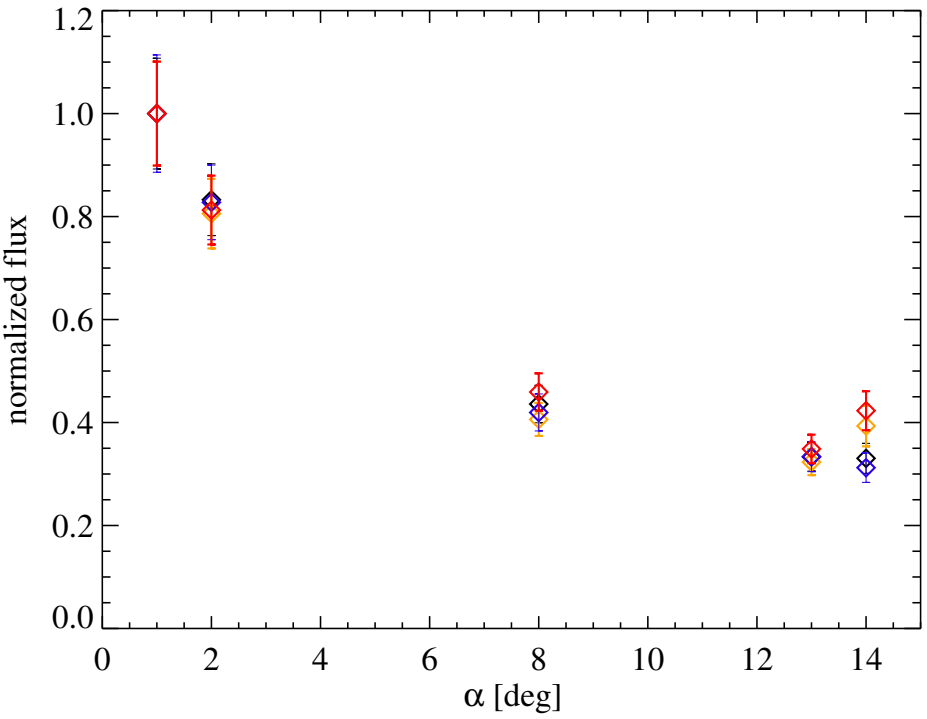

Fig. 2: Phase curve of the nucleus at low phase angles normalized at 1°. We report four different wavelengths: 0.55 μm (cyan), 0.80 μm (blue), 1 μm (yellow) and 2 μm (red). Error bars are from flux variability due to varying rotational phase.

2.3. Color ratios

The same dataset analyzed in sec. 2.1 and 2.2 has been used to compute color ratios at various wavelengths from integrated fluxes. Here we report three ratios as a function of the rotational phase (fig. 3): one in the VIS range ($C_{VIS} = (F_{0.55\mu m}/F_{0.8\mu m})/(F_{\odot,0.55\mu m}/F_{\odot,0.8\mu m})$), one in the IR ($C_{IR} = (F_{1\mu m}/F_{2\mu m})/(F_{\odot,1\mu m}/F_{\odot,2\mu m})$) and one across the VIS and IR ranges ($C_{VIS-IR} = (F_{0.55\mu m}/F_{2\mu m})/(F_{\odot,0.55\mu m}/F_{\odot,2\mu m})$). **Acquisition with solar phase angles ranging in the** $0° - 5°$ **interval have been selected.** It can be noted that C_{VIS}, C_{IR} and C_{VIS-IR} behave approximately as constants with no significative modulations. This indicates that surface spectral properties are fairly homogeneous on global scale at the spatial resolution of the dataset.

2.4. Geometric albedo

In this section we derive the geometric albedo of 67P/CG using the definition of normal albedo A_n. Normal albedo is the reflectance of a surface observed at 0° phase angle, normalized to the reflectance of a perfect lambert surface at null incidence angle. This quantity is not an integrated value and can be straightforwardly computed from the reflectance of full illuminated-pixels acquired at

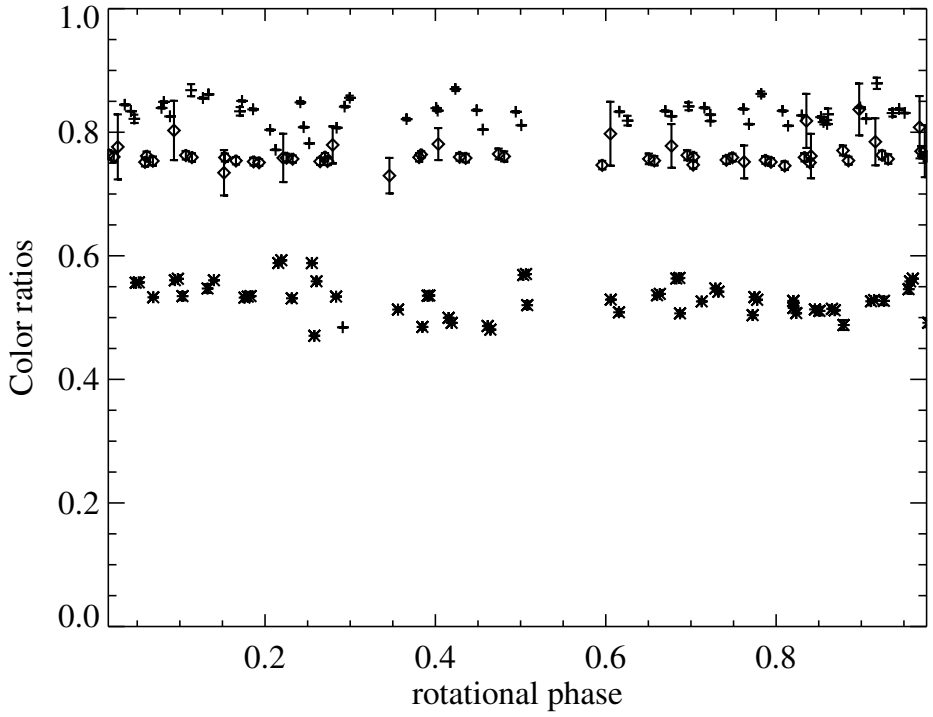

Fig. 3: Color ratios as a function of rotational phase. C_{VIS} is reported with diamonds, C_{IR} with crosses and C_{VIS-IR} with asterisks. **Error bars are typically smaller of the symbols size and the scatter of the points is due to the different solar phase angles of the single acquisitions.**

null α. Among the whole MTP005 observations dataset we selected pixels at the lowest phase angles ($1° - 2.5°$) and fully illuminated **(incidence and emission angles below** $10°$**)** as reported in fig. 4. An approximated linear trend of the I/F with phase angle can be recognized and by means of a linear fit we extrapolated the value at $\alpha = 0°$. The value obtained at 0.55 μm is $A_n = 0.062 \pm 0.002$ which is a refinement of the value previously reported in Capaccioni et al. (2015). In the approximation of single scattering, which can be safely applied to the case of a dark object like 67P/CG, the normal albedo turns out to have the same expression as the geometric albedo (Hapke 2012), the latter being the average value of the former over the illuminated portion of the target body. For this reason we assume that the value of A_n derived in this section matches the geometric albedo A_{geo} of the comet. **In order to compare our results to the ones derived in Fornasier & et al. (2015) we derived with the same technique described in this section the geometric albedo in the visible at wavelengths compatible with OSIRIS' filters. Because of larger noise affecting wavelengths shortward of 0.4** μm **and the presence of a spectral artifact in 0.8-1.0** μm **(see sec. 3.1.2) we limited the comparison to five wavelengths in the 0.4-0.8** μm **range, as reported in table 1. It can be noted the very good agreement between the results of the two instruments.**

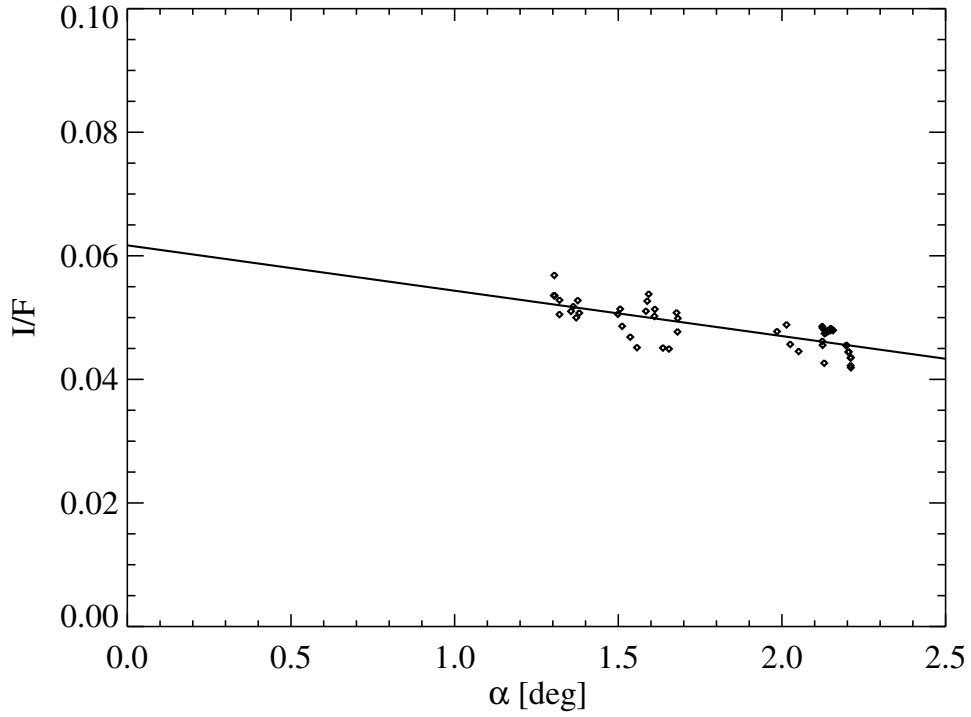

Fig. 4: Derivation of the normal albedo at 0.55 μm. The value at 0° is extrapolated by means of a linear fit as reported in the plot.

Table 1: **Geometric albedo of 67P/CG as measured by VIRTIS compared to OSIRIS.**

wavelength [μm]	A_{geo} **(This work)**	A_{geo} **(Fornasier & et al. 2015)**
0.480	0.054 ± 0.002	0.0554 ± 0.0024
0.535	0.059 ± 0.002	0.0589 ± 0.0034
0.649	0.073 ± 0.002	0.0677 ± 0.0039
0.700	0.077 ± 0.002	0.0720 ± 0.0031
0.743	0.080 ± 0.003	0.0766 ± 0.0031

3. Disk-resolved photometry

In this section data acquired during MTP006 to MTP12 sequences are analyzed. The CG nucleus spacecraft distance varies between 384 km and 7.7 km providing a spatial resolution from 96 m down to 1.9 m (see fig. 5), with most of the observations taken at a resolution below 25 m/pixel. Phase angle ranges in the 27.2° − 111.5° interval (see fig. 5) and different regions have been observed several times under varying observation geometries. In order to compare data acquired with different illumination conditions it is necessary to separate photometric effects from the spectral properties of the surface. This requires the necessity of a photometric reduction of the signal measured by VIRTIS to a quantity which is linked to the intrinsic brightness of the surface.

3.1. Photometric reduction

In order to compute a photometric reduction a model which links the reflectance of a particulate medium to the observation geometries and physical properties of the surface is required. There are

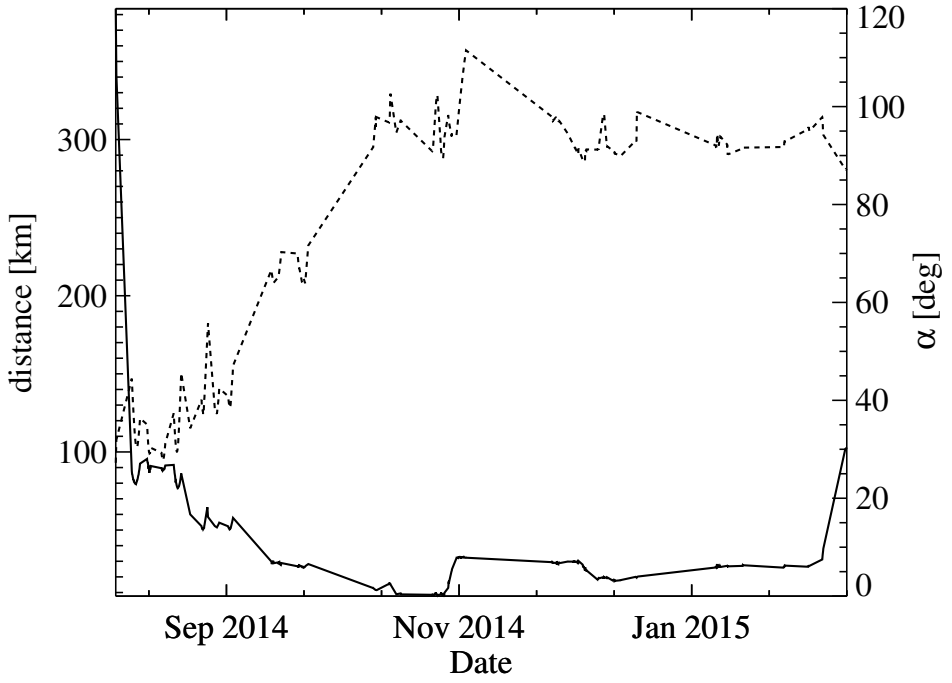

Fig. 5: Average target-spacecraft distance (solid line) and phase angle (dashed line) for the different VIRTIS-M acquisition.

several models, empirical, semi-empirical or physically based, which accomplish this task (Minnaert 1941; Akimov 1988; Shkuratov et al. 1999; Longobardo et al. 2014) and in this work we adopt the well-known Hapke's model (Hapke 1993, 2002, 2012). This solution of the radiative transfer equation has been extensively applied in planetary science to interpret data from remote sensing measurements (Domingue et al. 1995; Buratti et al. 2004; Ciarniello et al. 2011) and in particular to investigate photometric properties of cometary nuclei (Li et al. 2007b,a, 2009, 2013). The expression of the bidirectional reflectance of a semi-infinite medium from Hapke's model is given by the following equation:

$$r(i,e,\alpha) = \frac{w}{4\pi}\frac{\mu_{0e}}{\mu_{0eff}+\mu_{eff}}\left[B_{SH}(\alpha)p(\alpha) + H(w,\mu_{0eff})H(w,\mu_{eff}) - 1\right] \times S(i,e,\alpha,\bar{\theta})B_{CB}(\alpha) \qquad (2)$$

where:

- i, e, α: incidence, emission and phase angle
- w: single scattering albedo (SSA)
- $p(\alpha)$: single particle phase function (SPPF)
- μ_{0eff}, μ_{eff}: effective cosines of incidence and emission angle respectively
- $H(w,x)$: Chandrasekhar functions
- B_{SH}: shadow hiding opposition effect
- B_{CB}: coherent backscattering opposition effect
- $S(i,e,\alpha,\bar{\theta})$: shadowing function for large scale roughness

– $\bar{\theta}$: average surface slope

We refer to (Hapke 1993) for a complete description of every single term of eq.2. We want to mention that a refinement of the Hapke model, accounting for the effect of porosity, has been developed in Hapke (2008, 2012) and discussed in Ciarniello et al. (2014). However the vast majority of the photometric studies that use Hapke's theory applied the formulation given in eq. 2, which is the one used in this work in order to provide a direct comparison of our results with the ones derived in previous analyses.

Considering the lack of observations at low phase angles for the disk-resolved dataset $27.2° < \alpha < 111.5°$) and the extremely low albedo of comet surface (see sec. 2.4), the formulation given in eq.2 can be simplified posing to 1 the opposition effect terms B_{SH}, B_{CB} and the functions $H(w, X)$ which describes multiple scattering (single scattering approximation). Eq. 2 is then reduced to:

$$r(i, e, \alpha) = \pi I/F = \frac{w}{4\pi} \frac{\mu_{0eff}}{\mu_{0eff} + \mu_{eff}} p(\alpha) S(i, e, \alpha, \bar{\theta}) \tag{3}$$

where three quantities link the reflectance to the spectrophotometric properties of the surface: w, $p(\alpha)$ and $\bar{\theta}$. The SPPF is modeled following Heyney & Greenstein (1941)

$$p(\alpha) = \frac{1 - b^2}{(1 + 2b\cos(\alpha) + b^2)^{3/2}} \tag{4}$$

where b is the asymmetry parameter which determines the SPPF behavior:

– $b < 0$: backscattering

– $b > 0$: forward-scattering

The advantage of the formulation in eq. 3 is that, contrary to eq. 2, the photometric reduction is achieved by means of multiplicative term, thereby enabling the SSA to be computed in closed form, once the model parameters are determined. However, it must be pointed out that neglecting the contribution of multiple scattering in the modeling could introduce a limited overestimation of the retrieved w, while the elimination of the OE term, which should be negligible in the phase angle range used, could be, in principle, compensated by an adjustment of w, b. The whole dataset analyzed for the derivation of the photometric parameters has been filtered, in order to avoid unfavorable observation geometries due to large incidence and emission angles, imposing $i, e < 60°$ and pixels with extremely low reflectance (I/F < 0.001 at 0.55 μm). In particular this allow us to sort out pixels dominated by noise and minimize the number of residual partly-shadowed pixels not ruled out using the adopted nucleus shape model from Preusked et al. (2015) and to limit the effect induced by the error on the geometry. Concerning the latter point we recall that the relative error on $\cos(i)$ and $\cos(e)$ diverges when $i, e \rightarrow 90°$. This choice fixes the number of analyzed pixels to more than $2,100,000$. It represents a statistically representative sample of the global surface properties of the nucleus, also preserving acquisitions at large phase angle**, as shown in fig. 6, where the pixels density is reported in a I/F vs. α plot**. It can be noted that **the distribution develops** along a decreasing monotonic curve which links reflectance to phase angle, as expected.

Photometric reduction is computed under the assumption that photometric properties of the comet

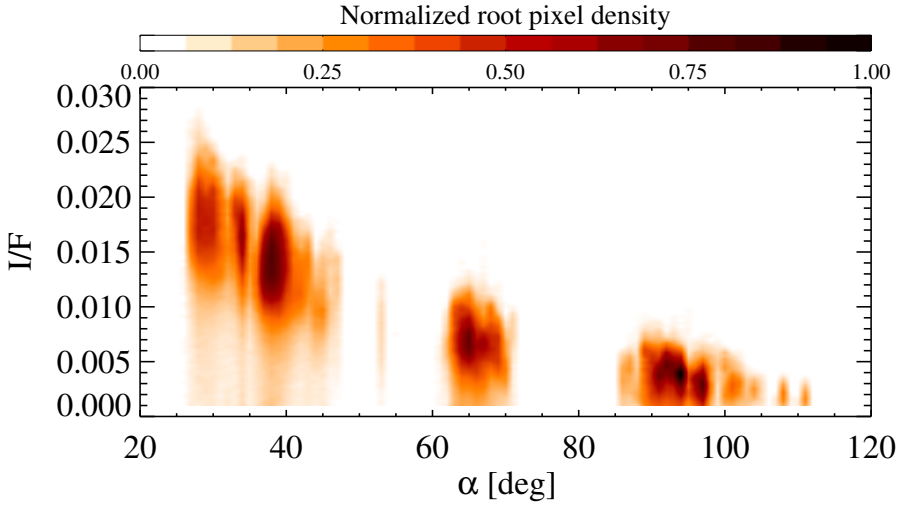

Fig. 6: a) I/F at 0.55 μm as a function of the phase angle**: contour plot showing points density.**

surface are globally homogeneous at the spatial resolution of VIRTIS observations. This implies that b and $\bar{\theta}$ are constant over the surface. As shown below in deriving b and $\bar{\theta}$ a determination of a global spectrum of w is obtained. This quantity can be considered as an average SSA spectrum of the comet. However we assume that most of the intrinsic brightness variability of comet surface is contained in the SSA. This allows, in a further step, to use the derived b and $\bar{\theta}$ into eq. 3 to estimate independently from each pixel a value of w, thus mapping the variation of albedo across the nucleus surface and to compare observations of the same regions acquired at different times along the comet orbit during the Rosetta mission.

In order to derive the set of Hapke parameters we applied the following iterative algorithm:

- the I/F at a given wavelength of each pixel is multiplied by the factor $4\frac{\mu_{0eff}+\mu_{eff}}{\mu_{0eff}S(i,e,\alpha,\bar{\theta}_0)}$ where $\bar{\theta}_0$ is a given value of the roughness slope parameter. Assuming eq. 3 this quantity represents $wp(\alpha)$ and we derive a distribution like the one shown in fig. 7
- the distribution of $wp(\alpha)$ is averaged in 1° phase angle bins
- the average curve of $wp(\alpha)$ is fitted, thus retrieving b and w
- the same procedure is repeated for all the VIRTIS wavelengths: residuals from selected wavelengths across VIS-IR are summed up
- the whole algorithm is repeated for $\bar{\theta}_0$ varying in the $[1° - 60°]$ range with 1° steps (fig. 8)
- the final $w, b, \bar{\theta}$ are selected as the ones that provide the minimum residuals

We recall that w and b in general are wavelength dependent quantities, while $\bar{\theta}$ is not, since it is linked to the morphology of the surface.

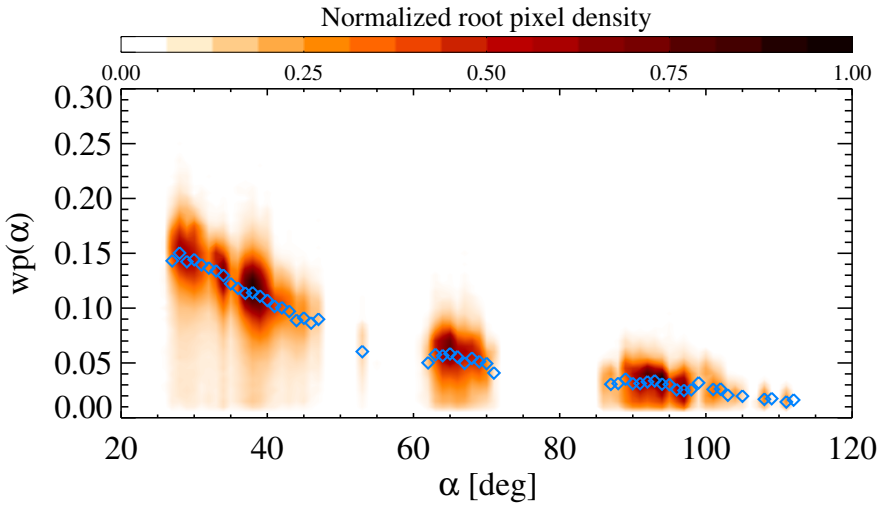

Fig. 7: $wp(\alpha)$ distribution at 0.55 μm as a function of phase angle for $\bar{\theta}_0 = 0°$. Blue diamonds represent the average values on 1° phase angle bins.

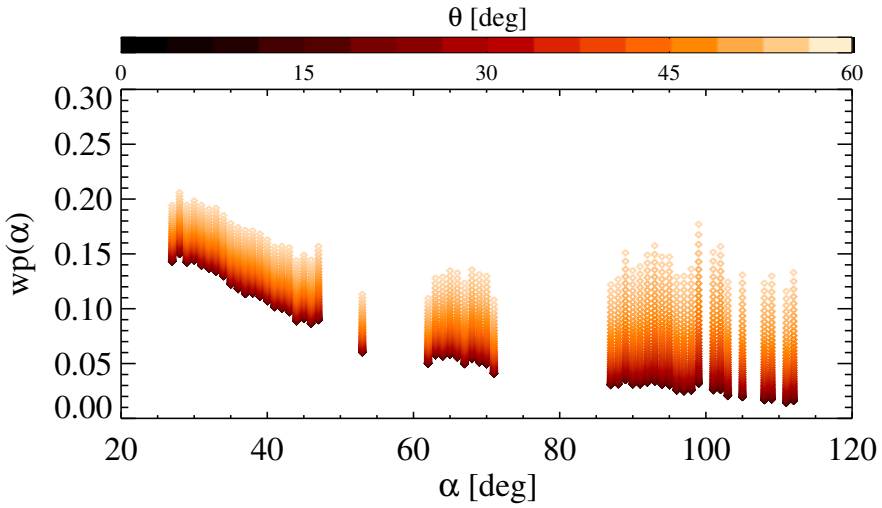

Fig. 8: $wp(\alpha)$ averaged on 1° phase angle bins for $\bar{\theta}$ varying in the 1° − 60° range. Color bar provides $\bar{\theta}$ values. Increasing roughness affects the estimated $wp(\alpha)$ inducing a flatter distribution with a larger overall level.

3.1.1. Surface roughness and $\bar{\theta}$

In fig. 9 we report the total residuals of the fitting procedure described in sec. 3.1 as function of $\bar{\theta}$. We compute this quantity with the following equation:

$$Res(\bar{\theta}) = \sum_{\lambda=0.55\mu m}^{2\mu m} \chi^2_\lambda(\bar{\theta}) \tag{5}$$

where $\chi^2_\lambda(\bar{\theta})$ is the resulting chi-square value of the fit of the average $wp(\alpha)$ curve derived assuming $\bar{\theta}$, at wavelength λ (fig. 8). Residuals have been summed in the $0.55 - 2\mu m$ range in order to exclude both shorter wavelengths, affected by larger noise, and longer ones, where thermal emission can partially be present even if not dominant. The minimum value of the residuals is obtained at

$\bar{\theta} = 19°$. The physical meaning of the surface slope parameter is still debated. While commonly related to the shadowing due to large scale roughness (Hapke 2012), laboratory studies from Shepard & Helfenstein (2011) point out that it can be affected by sub-mm scale structures. Moreover compensation effects with other photometric parameters in the fit procedure, as the asymmetry factor of SPPF and SSA, can also modify the retrieved value of $\bar{\theta}$, and this must be taken into account when interpreting its meaning. This effect could be important in the case of lack of observations at very large phase angles. Apart from these issues, we can give an estimate of the error on $\bar{\theta}$ by examining the curve in fig. 9: assuming the level of the first portion of the curve, which is not sensitive to the slope parameter, as a sensitivity threshold to the effects of the roughness, we can derive a final value of $\bar{\theta} = 19^{\circ}{}^{+4}_{-9}$.

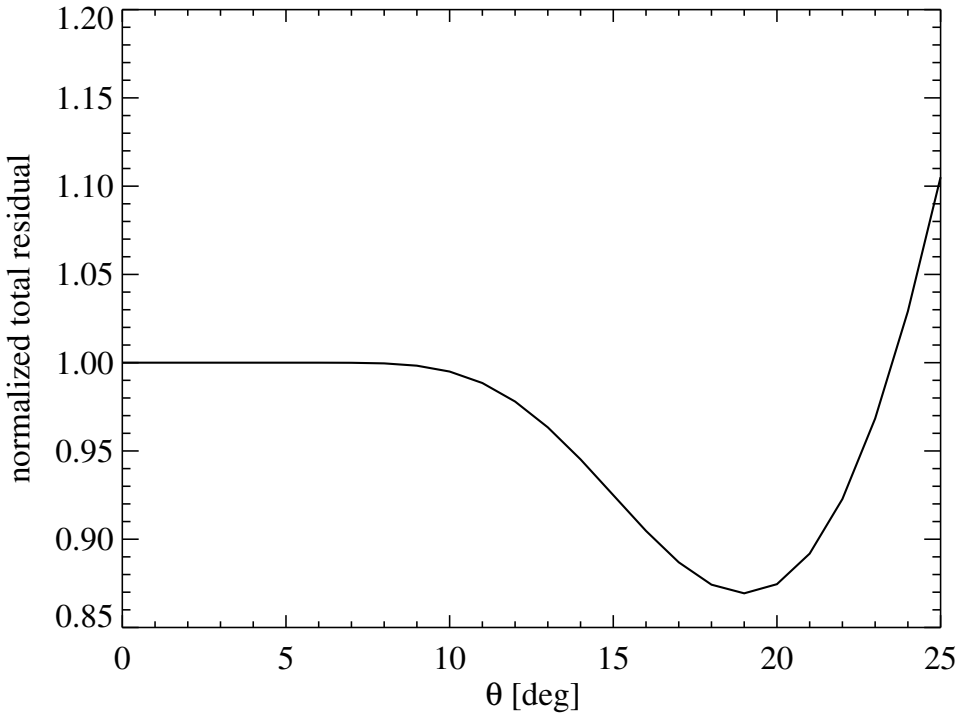

Fig. 9: Total residual as a function of the roughness slope parameter $\bar{\theta}$ normalized at $\bar{\theta} = 0°$.

3.1.2. SSA

In fig. 10 we report the derived spectrum of the single scattering albedo SSA. As shown previously in Capaccioni et al. (2015) the spectrum of the comet surface is reddish, with a steeper slope in the VIS region. The overall level of w is extremely low, with a value of 0.052 at 0.55μm, increasing in the IR up to 0.14 at 2.8 μm. The 3.2 μm absorption feature, caused by the presence of organic material, is clearly visible up to 3.5μm, where the thermal emission starts to affect the spectrum. A feature centered at 0.9 μm can be noted but it is currently interpreted as a residual artifact from calibration.

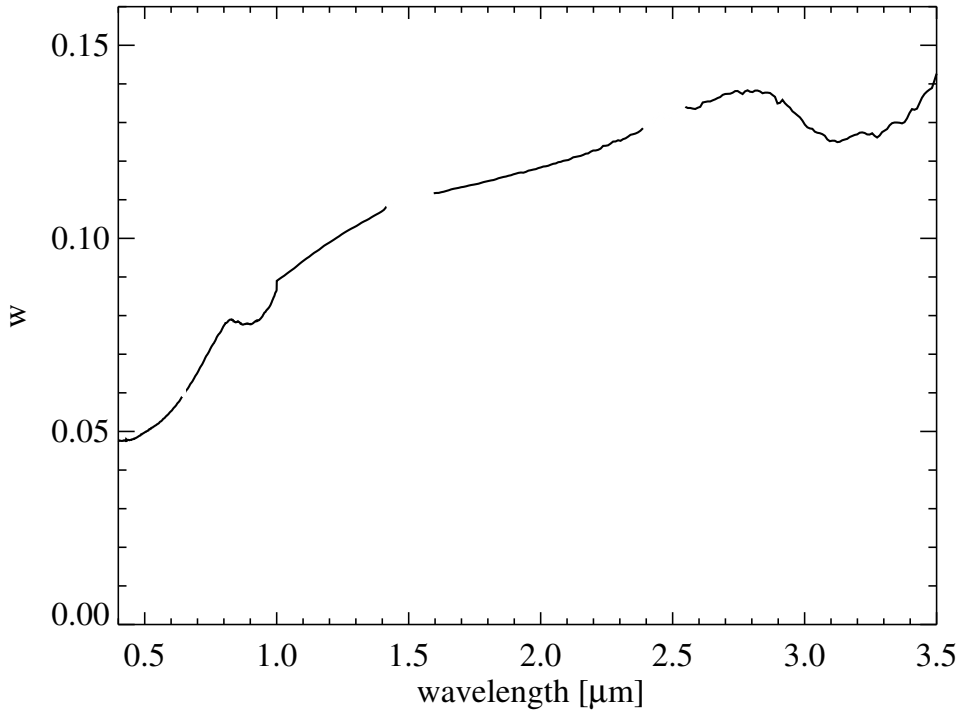

Fig. 10: Spectral variation single scattering albedo w (SSA) as derived from the computation of the photometric parameters. Missing parts of the spectrum are relative to instrumental spectral filters junction. The absorption in the 0.8-1 μm is a residual artifact from calibration.

As stated above the derived SSA can be considered as representative of the average properties of 67P/CG surface. However, spatial albedo variability is expected at VIRTIS observation scale, and this is the information we aim to extract after the application of the photometric reduction as shown in sec. 3.3.

3.1.3. SPPF

In fig. 11 we report the spectrum of the derived asymmetry factor b. The value at 0.55 μm is b=-0.42 indicating a strong backscattering behavior, as observed for other comets (tab. 3), slightly increasing with wavelength. As stated above, the asymmetry factor drives the behavior of the phase curve. The phase angle range investigated in this work albeit limited can be considered wide enough to provide a robust determination of b since it covers the portion of the phase curve most sensitive to this parameter. In fact, at very small and very large phase angles, the opposition effect and large scale surface roughness respectively dominate, masking the effect of the SPPF.

3.2. Comparison with Hapke modeling of OSIRIS data

Fornasier & et al. (2015), have applayed Hapke modeling to images of CG nucleus produced by the OSIRIS Narrow Angle Camera onboard Rosetta mission. Due to the better spatial res-

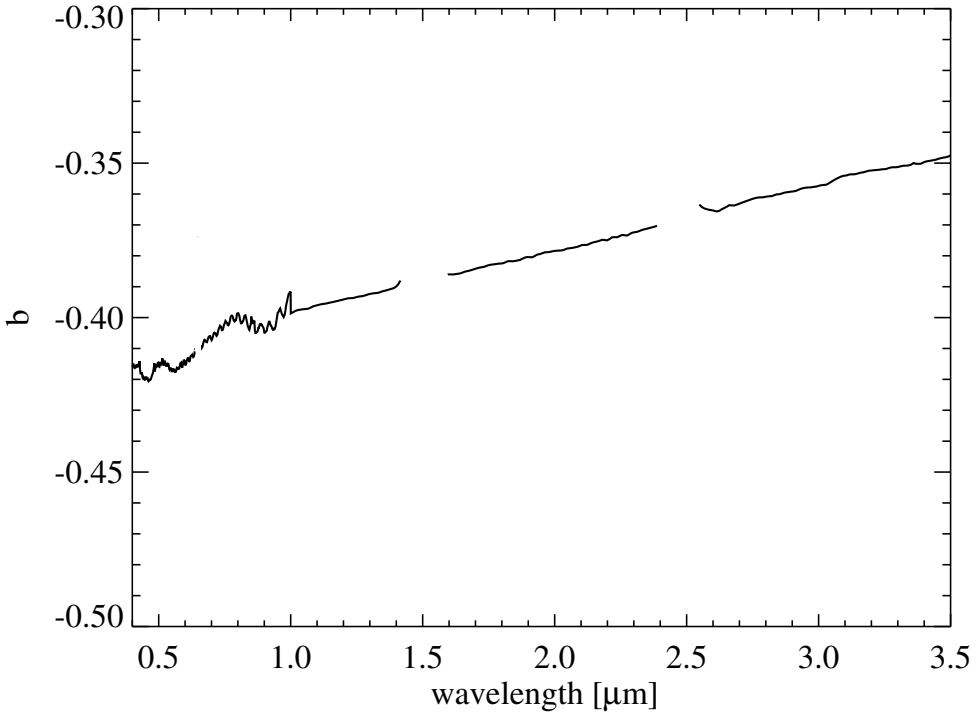

Fig. 11: Spectral variation of the asymmetry factor b as derived from the computation of the photometric parameters. Missing parts of the spectrum are relative to instrumental spectral filters junction.

Table 2: **Hapke modeling of 67P/CG nucleus photometric properties as derived by VIRTIS and OSIRIS data at 0.65 μm.**

Instrument	B_{0SH}	h_{SH}	B_{0CB}	h_{CB}	b	w	$\bar{theta}$
VIRITS (This work)	**-**	**-**	**-**	**-**	**-0.42**	**0.059**	19°
OSIRIS	**2.5**	**0.079**	**0.188**	**0.017**	**-0.37**	**0.042**	15°

olution with respect to VIRTIS (18.6 $\mu rad/pix$, Keller et al. (2007)) OSIRIS camera produced disk-resolved images of the CG nucleus during the MTP005 phase, whit solar phase angle down to 1.3°**. This made possible for Fornasier & et al. (2015) to characterize also the opposition effect region of the phase curve, determining the SHOE amplitude B_{0SH} and width h_{SH} and analogues parameters for the CBOE (B_{0CB} and h_{CB}). Two different Hapke models have been adopted Hapke (2002, 2012) the latter including the effect of porosity. Here we compare our Hapke modeling results with the ones obtained by OSIRIS for the Hapke (2002) case, which is more compatible with our approach. Results are summarized in table 2.**

Both the studies indicate a low SSA and a backscattering behavior of the $SPPF$. However it must be noted that in this work we obtain a larger value of the single scattering albedo and of the absolute value of b. This discrepancy is explained by the different version of the Hapke model which have been adopted. In particular, the inclusion of the OE in the model can account for part of the photometric output also at relatively large phase angles ($> 20°$) **thus requiring a smaller SSA and a less backscattering $SPPF$, as in the OSIRIS case. This**

effect can be important for very large values of B_{0SH} (> 1), where, in the case of backscattering surfaces the SHOE term on one side and the SPPF and the SSA on the other, can compensate, making difficult to disentangle between the two solutions. In this perspective CBOE plays a minor role, having smaller amplitude and angular width. We also retrieve a fairly larger value of the roughness slope parameter $\bar{\theta}$ in comparison to Fornasier & et al. (2015), and this is due to the fact that the dataset in the present work extends to larger solar phase angles (up to $111.5°$**) with respext to OSIRIS images (up to** $53.9°$**), thus being more sensitive to the effect of sub-pixel roughness.**

3.3. Accuracy of the photometric reduction and photometrically reduced data

Once the photometric parameters $(b, \bar{\theta})$ have been retrieved they can be applied to invert eq. 3 in order to derive the SSA from the I/F measured by VIRTIS for each acquired pixel on the surface. In fig. 12 we report the derived SSA at 0.55 μm after the application of the photometric reduction to all the pixels of fig. **??**. It can be noted that dependence on phase angle has been effectively

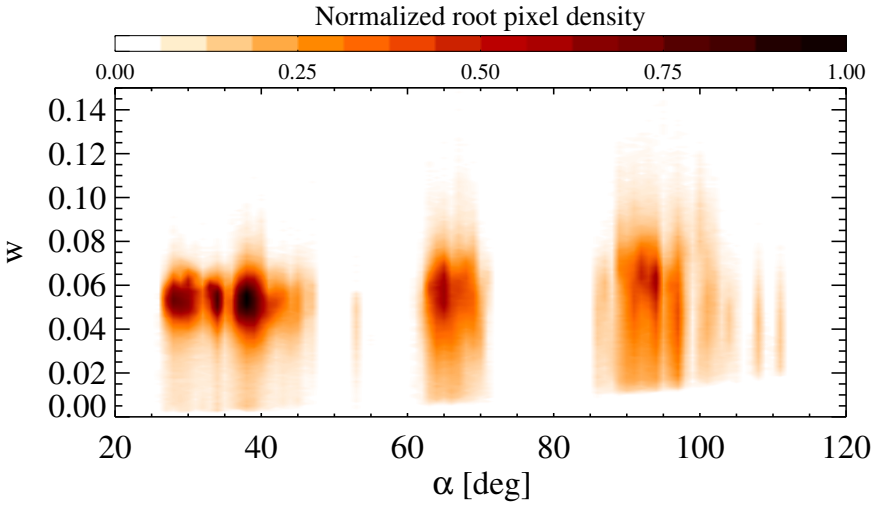

Fig. 12: Single scattering albedo at 0.55 μm vs. phase angle. Color bar indicates the root pixels density normalized at the maximum value. Correlation coefficient is $R_{w,g} = 0.03$

removed, as shown by the very low correlation coefficient ($R_{w,g} = 0.03$) and the cloud of values is distributed around the global value obtained in sec. 3.1.2 ($w = 0.052$). The width of the distribution at each phase angle is related to the intrinsic variability of the surface properties, to measurement error as well as to possible compensative effects generated by assuming a single determination of b and $\bar{\theta}$ for all the surface.

In fig. 13 we report the derived single scattering albedo values at 0.55 μm as a function of the incidence and emission angles. In both cases the SSA is substantially independent on i and e with $R_{w,i} = 0.03$ and $R_{w,e} = -0.05$ respectively.

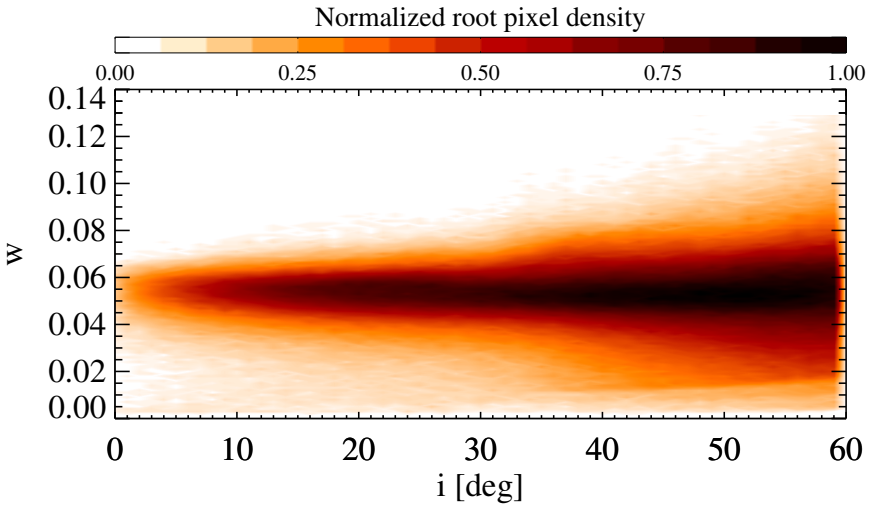

(a)

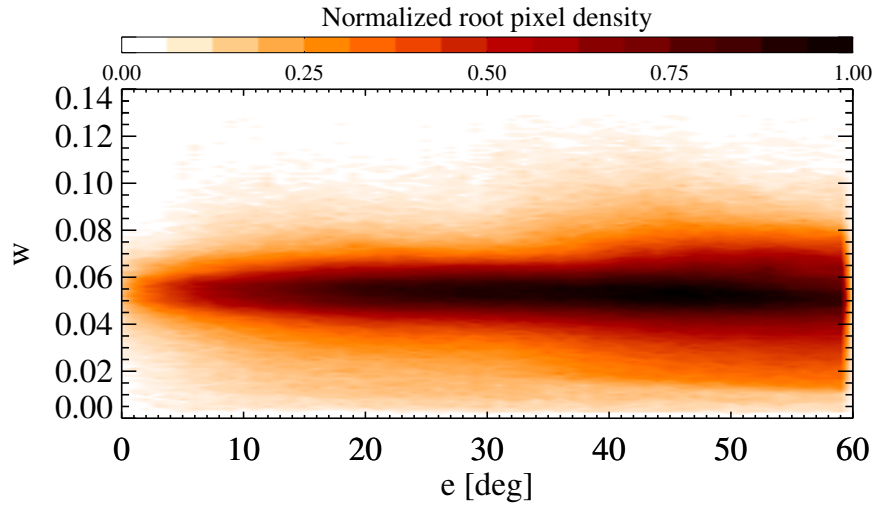

(b)

Fig. 13: Single scattering albedo at 0.55 μm vs. incidence angle (left panel) and emission (angle). Color bar indicates the root pixels density normalized at the maximum value. Correlation coefficient are $R_{w,i} = 0.03$ and $R_{w,e} = -0.05$ respectively.

In order to further check the accuracy of the derived photometric reduction we compare the I/F as measured by VIRTIS with the reduction factor rf:

$$rf = \frac{\mu_{0eff}}{\mu_{0eff} + \mu_{eff}} \frac{p(\alpha)}{4\pi} S(i, e, \alpha, \bar{\theta}) \tag{6}$$

As reported in fig. 14 these two quantities show a linear correlation which intercepts the origin, indicating that the photometric model we applied is appropriate to describe the reflectance of the surface of the nucleus. In particular the fitted slope coefficient is 0.052 and this quantity can be interpreted as the average single scattering albedo of the surface, confirming the value shown in fig. 10 at 0.55 μm. From fig. 14 it can be noted that no points with peculiar photometric properties can be isolated, indicating a certain homogeneity of the surface and this is confirmed in fig. 15

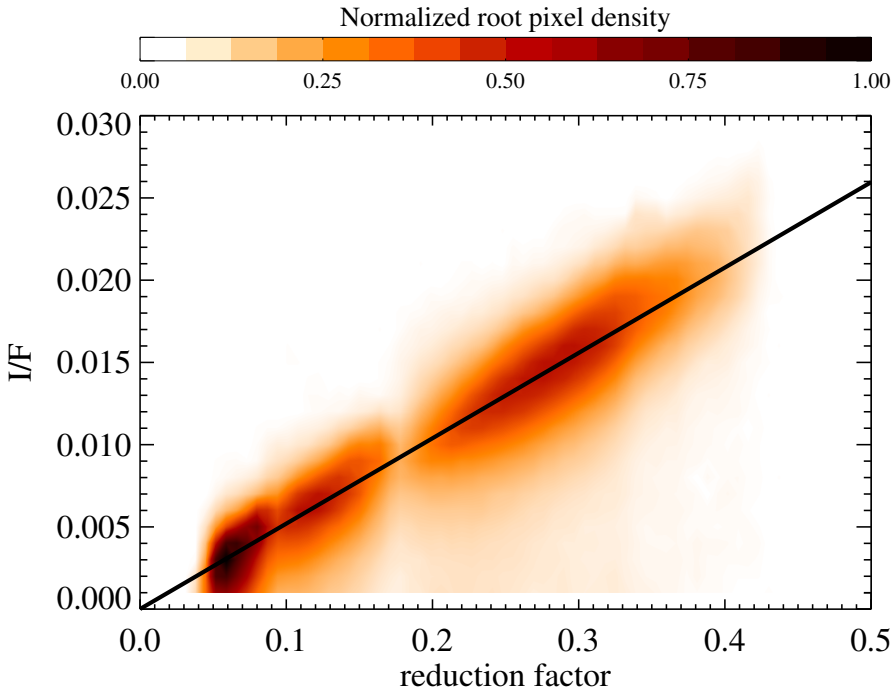

Fig. 14: I/F at 0.55 μm vs. the reduction factor. Color bar indicates the root pixels density normalized at the maximum value. Linear fit is reported as a black line with equation $I/F = 0.052 \times rf + 0.000033$.

where we report histograms of the derived w values at 0.55 μm and 1.8 μm. The two distributions are unimodal, meaning that at VIRTIS pixel scale we cannot recognize terrains with a statistically different behavior. Only an elongated tail towards low values of w can be found in both the distributions, possibly related to regions with lower albedo (see sec. 3.5) or residual partly shadowed pixels.

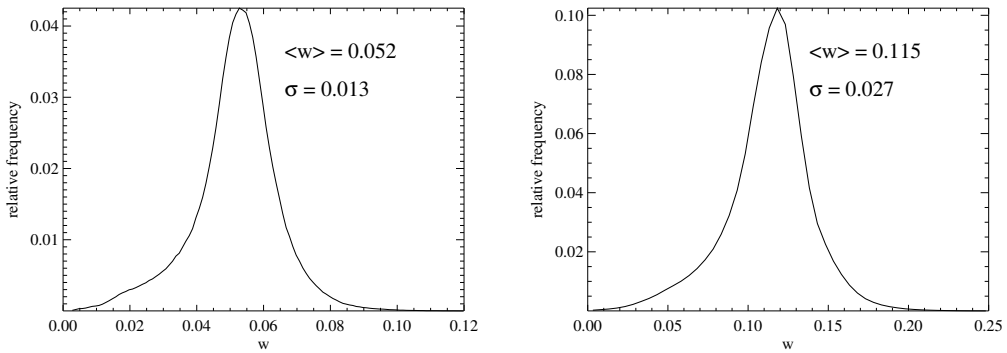

(a) (b)

Fig. 15: Histograms of the derived single scattering albedo at 0.55 μm (left) and 1.8 μm (right). Both the curves have been normalized at the total number of pixels. Mean values and standard deviation are reported in the plots.

In fig. 16 the result of the photometric reduction at 0.55 μm on typical VIRTIS hyper-spectral cubes is shown. Bright regions in I/F images disappear in the photometrically reduced ones, revealing similar SSA of the surrounding terrains. However in the reduced cubes residual of topography can still be recognized, due to the presence of shadows, as well as a mis-correction in correspondence of sharp reliefs, where the incidence and emission angle can be either large or abruptly varying at sub-pixel scale.

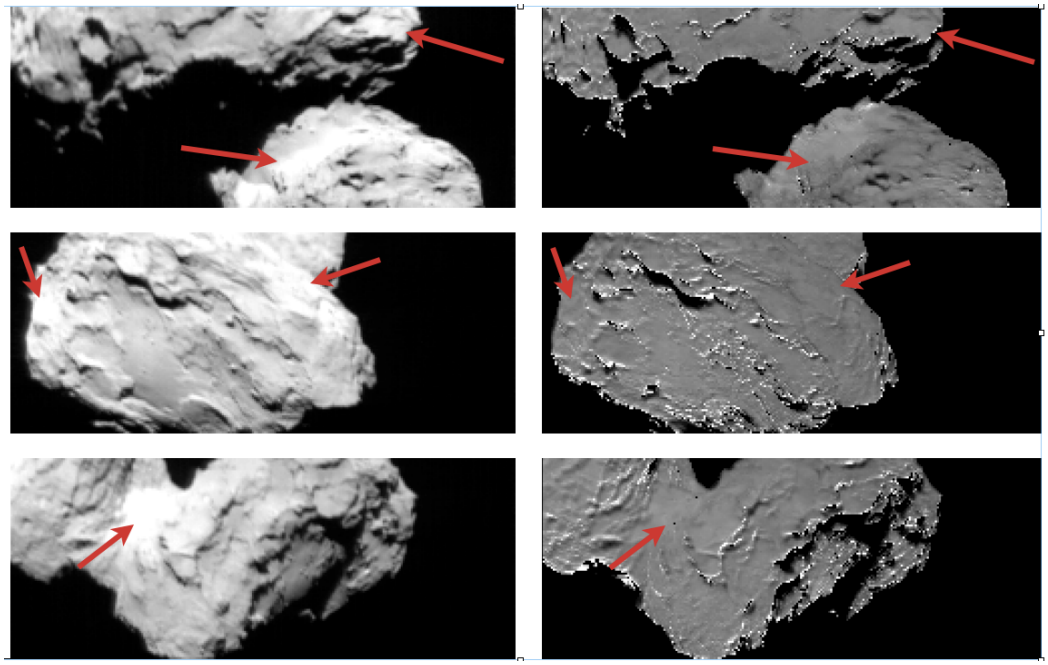

Fig. 16: I/F images (left) and w images after photometric reduction (right) at 0.55 μm. Red arrows indicate bright regions in the I/F images. The same regions in the photometrically corrected images show a single scattering albedo level compatible with the one of the surrounding terrains, revealing that I/F brightness enhancement is due to observation geometry.

3.4. Spectral slopes and phase reddening

In fig. 17a and 17b we report the spectral slope as a function of the phase angle in two ranges: between 0.55 μm and 0.80 μm ($S_{VIS} = \frac{I/F_{0.80\mu m} - I/F_{0.55\mu m}}{I/F_{0.55\mu m}(8k\text{Å} - 5.5k\text{Å})}$) and between 1 μm and 2 μm ($S_{IR} = \frac{I/F_{2\mu m} - I/F_{1\mu m}}{I/F_{1\mu m}(20k\text{Å} - 10k\text{Å})}$). It can be noted that spectral slopes in the two intervals increase with phase angle. This phenomenon, typically referred to as phase reddening, is common to many planetary bodies, like asteroids (Clark et al. 2002), icy satellites (Filacchione et al. 2012) and planetary rings (Filacchione et al. 2014) and has been also observed in laboratory measurements (Schröder et al. 2014). From the linear fits reported in fig. 17a and fig. 17b we obtain respectively values of relative phase reddening of 0.44%/° in the VIS and 0.73%/° in the IR. The finding of a pronounced phase reddening is also reported in Fornasier & et al. (2015) from OSIRIS camera onboard Rosetta**, where they measure a relative phase reddening in the VIS of the order of** 0.95%/°**. This value is larger with respect to the one derived in the present work, however it has been computed on a slightly different wavelength interval (0.535** μm **- 0.882** μm**) and within a different solar**

phase angle range $1.3° - 53.9°$**. This latter argument can explain the difference among the two measurements, since phase reddening intensity can vary with phase angle as shown in Schröder et al. (2014).** In fig. 17 we also report the same quantities after the photometric reduc-

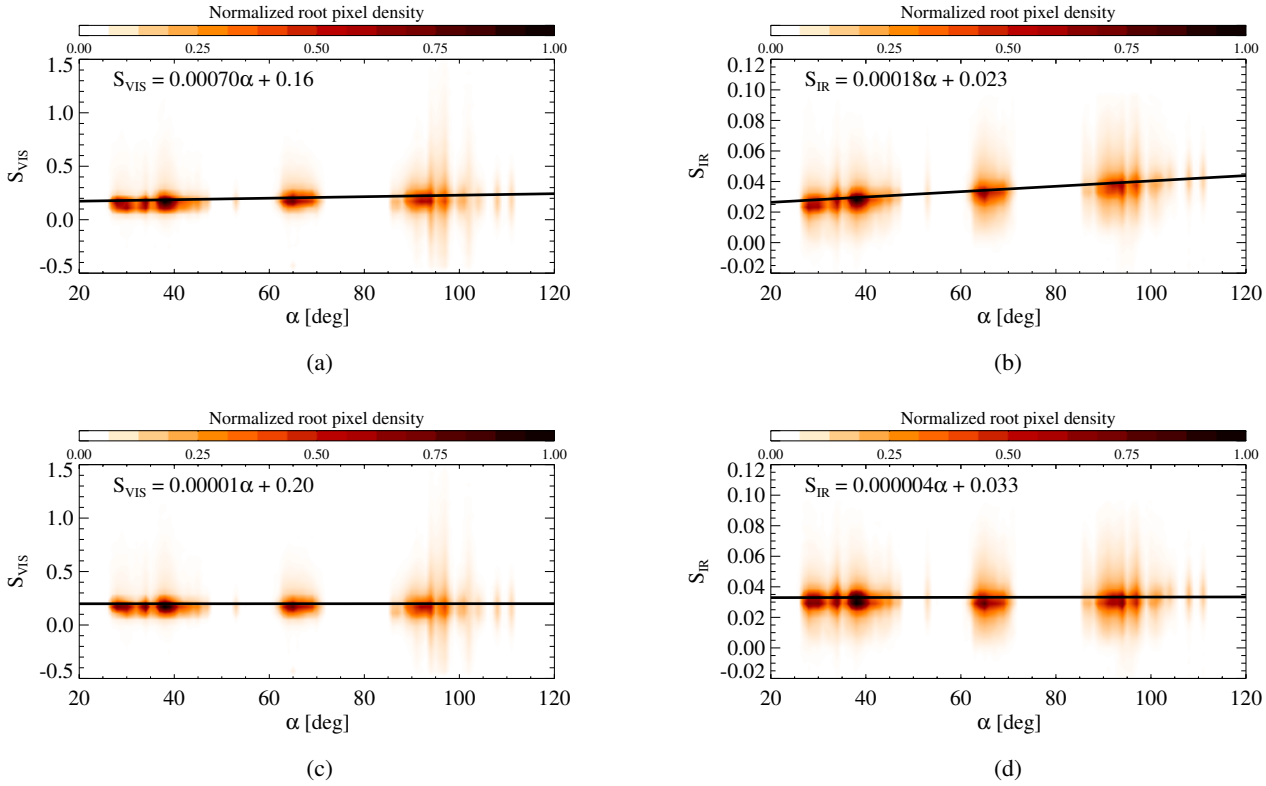

Fig. 17: Density plot of the spectral slope in the VIS range (a) and IR (b) range as a function of the phase angle. The same quantity, after photometric reduction, is reported in (c) and (d) for VIS and IR respectively. Linear fits are reported as a black line in the plots.

tion and it can be noted that dependence on phase angle has been basically removed, with final values of $S_{VIS} = 20\%/k\text{Å}$ (fig. 17, bottom left) and $S_{IR} = 3.3\%/k\text{Å}$ ((fig. 17, bottom right)). This quantities confirm the previous measurements of spectral slopes reported in (Capaccioni et al. 2015).

Phase reddening can be interpreted as an effect of multiple scattering (Cuzzi et al. 2002; Li et al. 2015), which is relatively more important at large phase angles for bodies with backscattering phase function, by stretching albedo differences at different wavelengths. This explanation is reasonable for surfaces with moderate-large w, where multiple scattering plays an important role, but may be not sufficient in the case of dark surfaces, where single scattering is the dominant process. In the photometric modeling presented so far we neglected multiple scattering; however, our photometric reduction to w removes phase reddening because the derived single scattering phase function behavior varies with wavelength (fig. 11). It is then legitimate to wonder if this result is just a compensation effect due to our simplified model. In order to test this hypothesis we computed I/F simulated slopes in the VIS and IR applying a Hapke model including multiple scattering, with SSA values as derived by our analysis but with constant values of the asymmetry factor in

each spectral range $b_{VIS} = -0.42$ and $b_{IR} = -0.40$, compatible with the ones we determined so far, for all the observation geometries of our dataset (fig. 18).

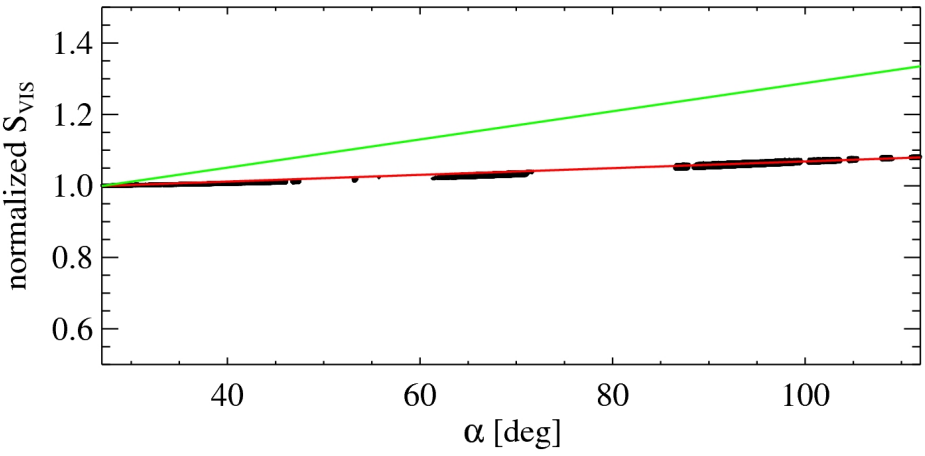

(a)

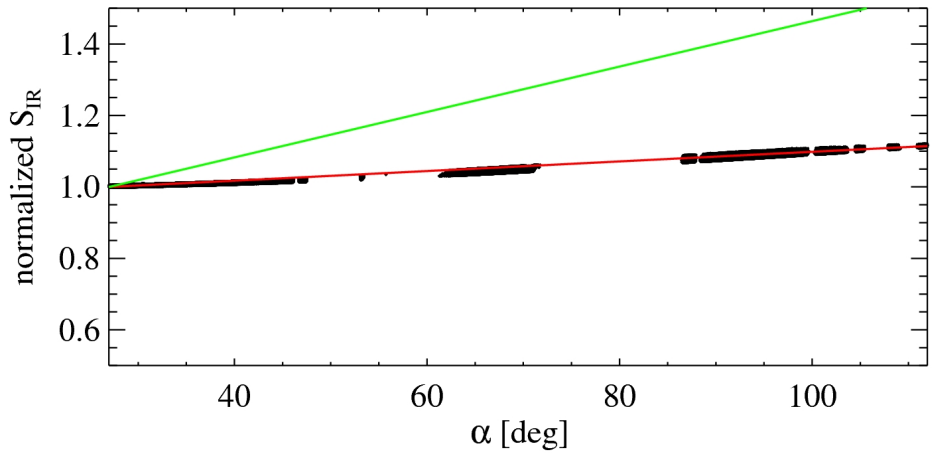

(b)

Fig. 18: S_{VIS} (a) and S_{IR} (b) normalized at the smallest phase angle as a function of g. Black points are simulated values as described in the text, red curve is their linear fit and the green curve is the linear fit of the measured spectral slope distribution of CG comet (fig. 17).

This allows to estimate at which extent phase reddening can be due to multiple scattering when the single scattering phase function is constant over the wavelength range. The values of phase reddening we obtain from a linear fit (red curve) of the simulated I/F distribution of fig. 18 are respectively $0.1\%/^\circ$ for VIS and $0.14\%/^\circ$ for the IR, well below the ones we measure from VIRTIS observations. This indicates that, for 67P/CG and in more general terms low-albedo surfaces, multiple scattering is not sufficient to explain phase reddening and in particular single scattering is the dominant process. This also shows that the simplified Hapke model we adopted well describes CG photometric properties.

Such a monotonic phase reddening has been measured and simulated by Schröder et al. (2014) for

opaque material where single scattering is significative. They suggest this effect can be related to the roughness on the surface of the particles composing the regolith combined to a positive spectral slope of the reflectance. This is compatible with our finding of a phase reddening related to the single scattering process. In fact the SPPF, along with SSA, describes the average scattering property of the particle and the behavior we derive (fig. 11) can account for the effect of particle surface roughness.

3.5. Albedo maps

The derived SSA values (see fig. 12) have been reprojected, according to their coordinates, onto a cylindrical map with a grid of 1° sampling both in longitude and latitude. In the case of more than one value located in the same cell we computed the median. The result of this approach are single scattering albedo maps of the surface, and in fig. 19 we report two examples at 0.55 μm and 1.8 μm. This allows to investigate local photometric variability that cannot be appreciated from the global analysis presented so far, being masked in the SSA albedo distribution derived in fig. 15. In order to give a reference to the reader we divided the nucleus **in** four macro-regions **(fig. 19c)**: head, neck, body and bottom. In the 0.55 μm map **(fig. 19a)** it can be noted that the neck region, which corresponds to the Hapi area of Thomas et al. (2015), and the center of the bottom region (Imothep in Thomas et al. (2015)) have a relatively larger single scattering albedo with respect to the rest of the comet, as found by Fornasier & et al. (2015), while in the middle of the body region, approximately at $150° < lon < 180°$, $40° < lat < 60°$ a darker area can be observed. Some residual of topography is still present, which produces the small scale variations of the albedo, due to the effects of partly-shadowed pixels or mis-correction in the correspondence of sharp reliefs. A similar result is obtained in the case of the map at 1.8 μm **(fig. 19b)**. In this case the Imothep plain appears even brighter than the neck, indicating a a slightly redder SSA across the VIS-IR. This is confirmed in fig. 20, where a RGB composite map is shown from data at 0.44 μm (blue), 0.55 μm (green) and 0.70 μm (red). A dichotomy of the nucleus surface can be noted, being redder in correspondence of the bottom, body and head regions, while the neck area shows a more neutral spectrum. This difference has not emerged from the full-disk photometric analysis (sec. 2.3) because of the limited extension of the neck region as well as its position, frequently shadowed by the two main lobes of the nucleus.

3.6. Zonal photometric reduction

In this section we investigate separately the four macro-regions described in sec. 3.5 deriving an independent photometric reduction for each one. This approach has the twofold advantage of providing a more accurate photometric reduction for each region and exploiting, if present, global scale differences in the spectrophotometric properties of the surface, which could have been masked in the previous analysis. In fig. 21 we report the derived asymmetry parameter b and the w for the four macro-regions. It can be noted that both the derived spectra of b and w are respectively similar to

the ones derived in the case of the global analysis of 3.1. The retrieved surface roughness parameters are $\bar{\theta}_{head} = 21°$, $\bar{\theta}_{neck} = 18°$, $\bar{\theta}_{body} = 20°$ and $\bar{\theta}_{bottom} = 18°$. Major differences with respect to the average properties of the nucleus are seen for the neck and the bottom region. In the first case the derived parameters indicate a more backscattering SPPF and a deeper absorption feature at 3.2 μm, with the minimum shifted at 3.1 μm. The increased band depth at 3.2 μm and the shift of the minimum of the can be due to an enrichment of water ice which could also be related to the fact that the most of the activity is related to the region of the neck and surroundings at the time of these observations (Sierks et al. 2015). The bottom region, on the other side, shows the highest albedo in the IR. The derived roughness parameters are similar among the different regions and to the global value $\bar{\theta} = 19°$. This apparently contradicts the fact that the neck (Hapi) and the bottom (which includes the Imothep plain) are characterized by smooth terrains as shown by OSIRIS images (Thomas et al. 2015), thus pointing to a link of the slope parameter with millimeter scale roughness.

4. Connecting full-disk and disk-resolved images

In this section we present an attempt to retrieve a complete phase curve of the comet in the Bessel V band (Bessell 1990) by connecting both full-disk and disk-resolved data. For this purpose we are following a classical approach in which the shape of the nucleus is assumed spherical: since the real shape is indeed not spherical, the accuracy of the resulting phase curve is limited by this assumption. The relative magnitude is determined from the integrated flux by means of eq. 1. This is not possible in the case of disk-resolved images because a measurement of the integrated flux is not available. However, assuming that the nucleus is spherical we can derive the flux from the comet in the V band from the following equation:

$$F_{CG,V} = F_{\odot,V} \frac{< I/F >_{\alpha,V}}{\pi} \frac{\pi R^2 \Phi(\alpha)}{\Delta^2} \tag{7}$$

where $F_{\odot,V}$ is the solar flux, $< I/F >_{\alpha,V}$ is the average reflectance at phase angle α from the dataset of disk resolved images, R is the comet equivalent radius, $\Phi(\alpha) = \frac{1+\cos(\alpha)}{2}$ is the fraction of the surface both visible and illuminated and Δ is the spacecraft-comet distance. Given this, it is then possible to retrieve the reduced magnitude $V(1, 1, \alpha)$ by applying the second and third expression of eq. 1. In fig. 22 we report the phase curve we obtained by combining the full-disk and disk-resolved datasets. The equivalent comet radius $R = 1.72\ km$ has been estimated as the radius of a sphere having the same volume of CG comet which is $21.4 \pm 2.0\ km^3$ (Sierks et al. 2015). At small phase angles the OE peak is fully developed while at larger α the magnitude increases linearly. This ideally divides the curve in two regions with different linear phase coefficients which have been fitted with the following results: $\beta_{\alpha<15°} = 0.077 \pm 0.002\ mag/°$ and $\beta_{\alpha>15°} = 0.041 \pm 0.001\ mag/°$. We can compare $\beta_{\alpha<15°}$ with previous measurements provided by Tubiana et al. (2011) with compatible phase angle coverage and the values are in good agreement being the latter in the 0.061-0.076 $mag/°$ range. With respect to other Jupiter-family comets the value we retrieve is

slightly larger than the average $\beta = 0.053 \pm 0.005\ mag/^\circ$ which has been derived by Snodgrass et al. (2011). **Fornasier & et al. (2015) computed a linear fit considering only points with** $7^\circ < \alpha < 54^\circ$ **deriving** $\beta = 0.047 \pm 0.002\ mag/^\circ$**. This quantity is comparable to** $\beta_{\alpha>15^\circ}$ **derived in this work. The two quantities are slightly different but it must be considered that the covered phase angle ranges are not the same between the two datasets and that our measurement assumes, for this phase angle range, a spherical nucleus. Fornasier & et al. (2015) also derived the slope for** $\alpha < 7^\circ$ **obtaining** $\beta = 0.074\ mag/^\circ$ **which is in perfect agreement with** $\beta_{\alpha<15^\circ}$ **computed in this work. In order to further characterize the CG phase curve we applied the HG formalism (Lagerkvist & Magnusson 1990) to fit** $V(1, 1, \alpha)$**. We obtained for the absolute magnitude** $H_V(1, 1, \alpha) = 15.7 \pm 0.1$ **and for the slope parameter** $G = -0.10 \pm 0.04$ **which are both in good agreement with the values from OSIRIS measurements (Fornasier & et al. 2015),** $H_V(1, 1, \alpha) = 15.74 \pm 0.2$ **and** $G = -0.13 \pm 0.01$**.**

5. Comparison to other comets

Before the Rosetta mission 5 comets have been imaged from instruments onboard spacecraft: 1P/Halley (Giotto), 9P/Tempel 1 (Deep Impact), 19P/Borrelly (Deep Space 1), 81P/Wild 2 (Stardust mission) and 103P/Hartley 2 (EPOXI). In this section we compare the photometric properties we derived for 67P/ Churyumov-Gerasimenko with the ones derived for these comets and with previous measurements of CG. In particular here we compare color indices $B-V$, $V-R$, $R-I$, the SSA, the asymmetry parameter b and the geometrical albedo A_{geo} at 0.55 μm, the roughness parameter $\bar{\theta}$ and the linear phase coefficient β. The results are summarized in tab. 3. Color index values of CG have been computed, in this work, after the photometric reduction has been applied. This means that we assume the flux of the comet proportional to the retrieved SSA. As shown in sec. 3.4 the effect of phase reddening has been eliminated and this must be considered in the comparison with color indexes from other works, which are typically derived at a given observation geometry: generally low phase angles for ground based observations and variable phase angles for measurements from spacecraft. It can be noted that the retrieved values of $B-V=0.73$ and $V-R=0.57$ are compatible with values of other comets. In particular there is a good agreement with previous CG measurements by Tubiana et al. (2011) and Lamy et al. (2006). Concerning the $R-I$ color index, our value of 0.59 is the largest among the comets reported in tab. 3 and in particular it must be noted that it is not compatible with the one of Tubiana et al. (2011), thus requiring further investigation. The values of the 67P/CG SSA is 0.052 at 0.55 μm (from distribution of fig. 15a), larger than most of the values derived for other comets but still indicating a very dark object, which appears to be a common property of cometary nuclei. The value derived in Fornasier & et al. (2015) from disk-averaged analysis is $w=0.037$, but in their Hapke modeling OE is included and a lower value of the roughness parameter is assumed **(sec. 3.2)**. The asymmetry parameter $b=-0.42$ at 0.55 μm indicates a backscattering SPPF, very similar to the other values reported in tab. 3 and in perfect agreement with the value of Fornasier & et al. (2015). Roughness slope parameter is comparable to other results, all indicating moderate to large topographical variegation, while the derived geometric albedo of CG at 0.55 μm is an intermediate value in this family of cometary nuclei and our determination is in agreement with Sierks et al. (2015). Finally, we obtained two values of the linear phase coefficient, one for $\alpha < 15^\circ$ and one for $\alpha > 15^\circ$. As already mentioned, our determination at low phase angles is comparable with observation conditions of Tubiana et al. (2011) **and the derivation of Fornasier & et al. (2015) at $\alpha < 7^\circ$ providing good agreement. Conversely, at large phase angles, our $\beta = 0.041 \pm 0.001 mag/^\circ$ is the lowest of the entire set of values reported here. Fornasier & et al. (2015) finds an intermediate value in the phase angle range $7^\circ < \alpha < 54^\circ$, close to our determination but outside the error bars. We must recall, in this context, that the phase angle coverage plays an important role in determining the final value of β, and moreover our determination relies on the strong assumption of a spherical shape of the comet. This makes a direct comparison with other measurements difficult.**

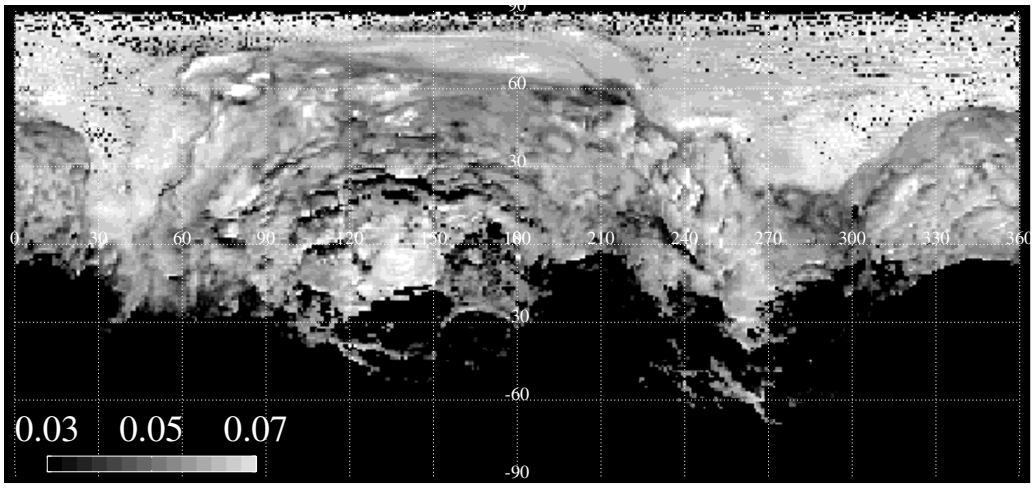

(a)

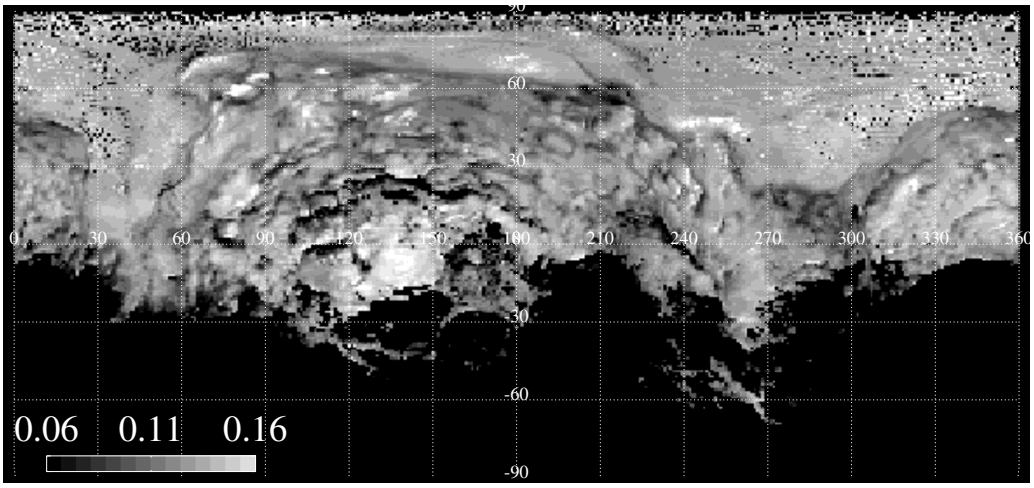

(b)

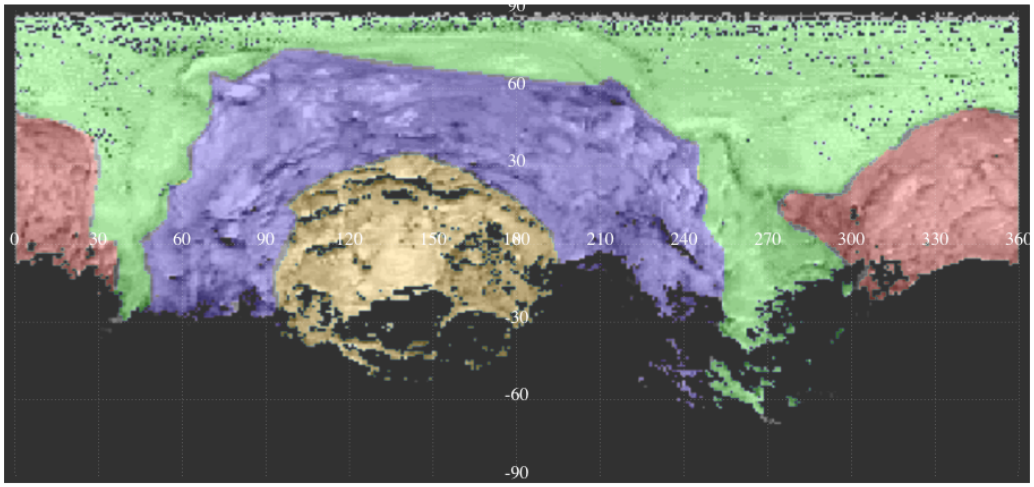

(c)

Fig. 19: (a) SSA map at 0.55 μm. (b) SSA map at 1.8 μm. **(c) The four macro-regions superimposed on the SSA albedo map: head (red), neck (green), body (blue) and bottom (orange).**

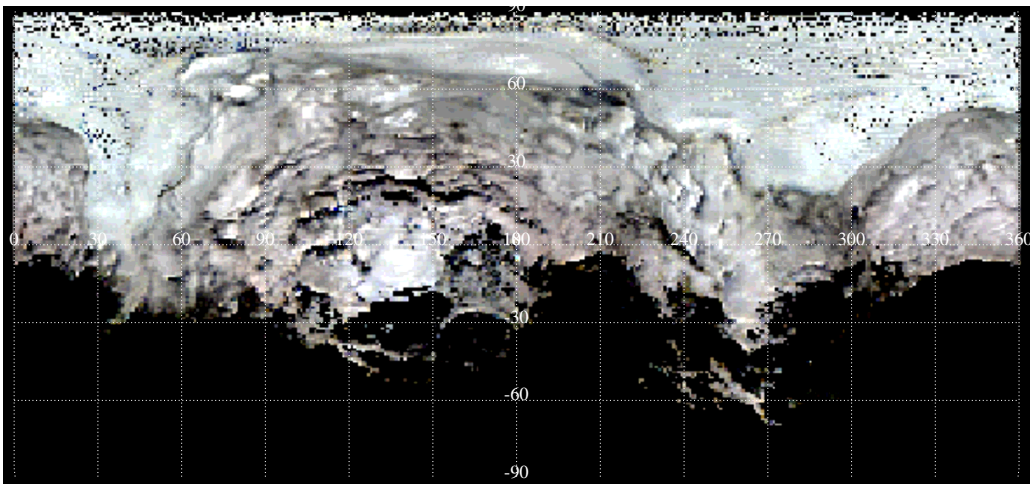

Fig. 20: Red (0.70 μm), green (0.55 μm) and blu (0.44 μm) SSA map.

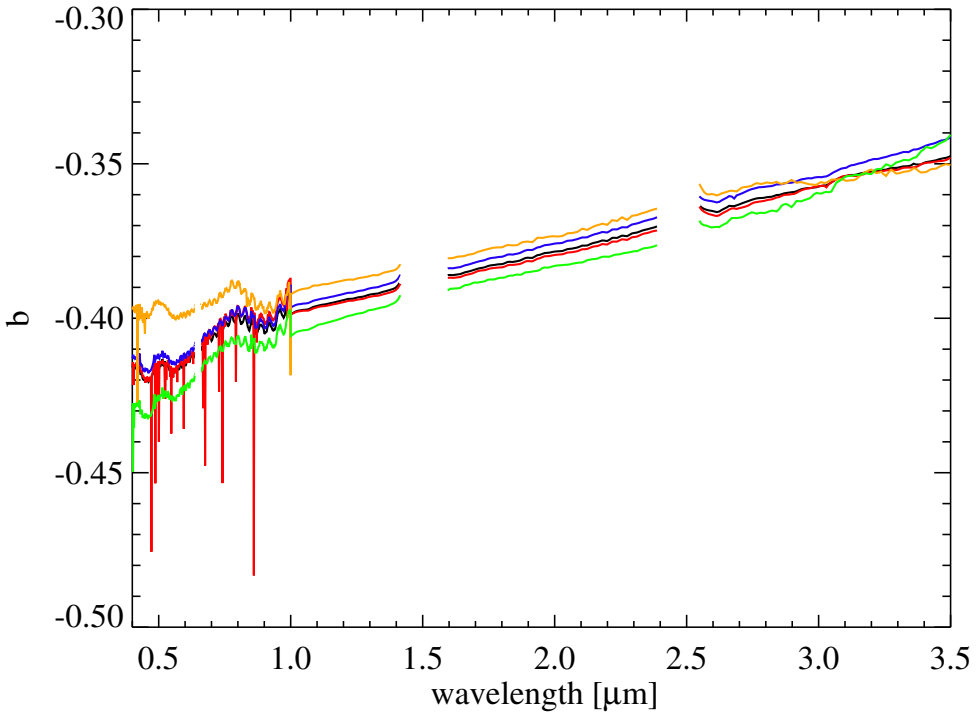

(a)

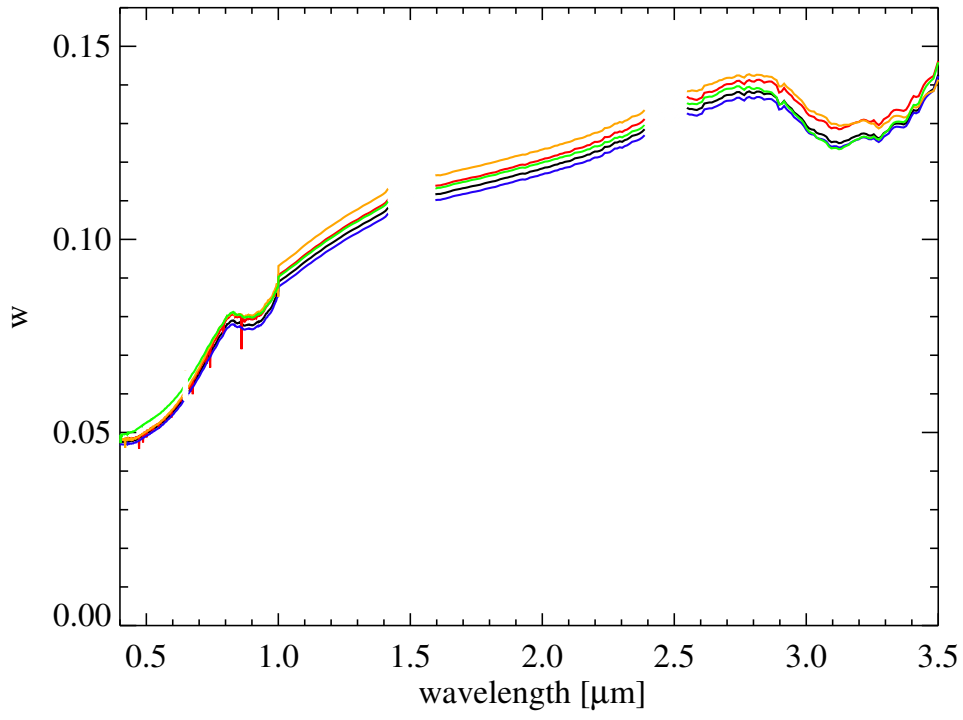

(b)

Fig. 21: Spectral variation of b (a) and w (b) for the four different macro-regions: head (red), neck (green), body (blue) and bottom (orange). The derived spectra from the global analysis are reported in black. The absorption common to all the spectra in the 0.8-1 μm is likely a residual artifact of calibration. Some abrupt oscillations of both w and b at certain wavelengths are due to degeneration in the fitting.

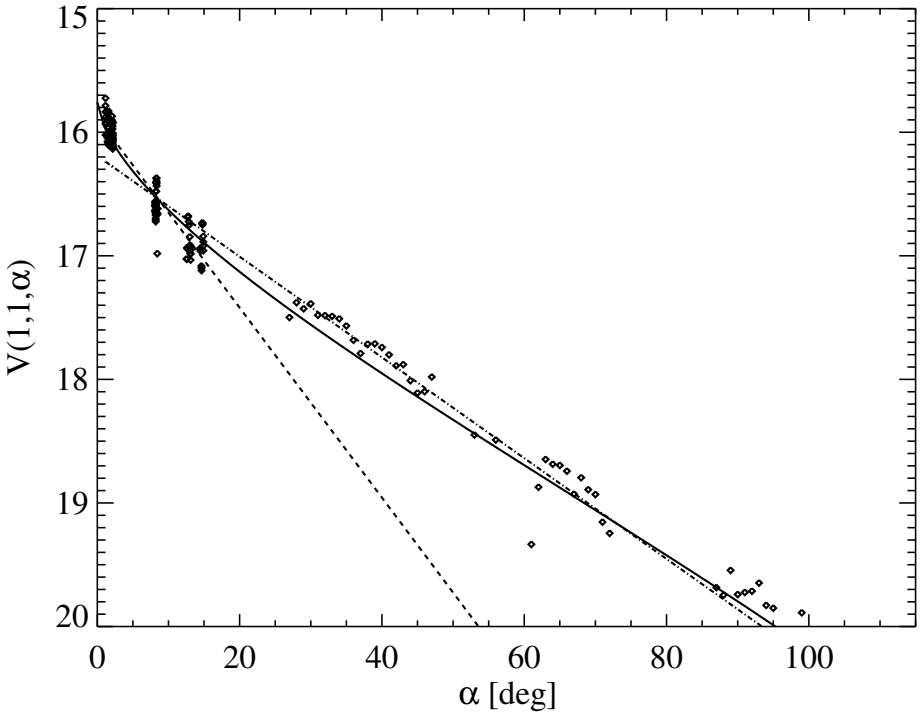

Fig. 22: V band phase curve. Points with $\alpha < 15°$ are from full-disk images while points with $\alpha > 15°$ are from disk-resolved data averaged on 1° bins. Dashed and dot-dashed lines represent respectively linear fits of $\alpha < 15°$ and $\alpha > 15°$ data points. **Solid line is the fitted HG curve. Computed errors are typically smaller with respect to the observed scatter of the points, and are not reported on the plot being not representative of the real uncertainty. For points at $\alpha < 15°$, which correspond to integrated fluxes from VIRTIS data, the scatter of the points is due to the variable projected cross section of the comet between the different observations. At larger solar phase angles the flux is computed from the average value of the I/F at each given phase angle. The corresponding error, derived as the standard deviation of the I/F distribution at each α normalized to the root of the number of elements in that phase angle bin, is much smaller than the observable scatter, indicating a non gaussian behavior.**

Table 3: Spectrophotometric properties and Hapke parameters of 67P/CG compared to other cometary nuclei.

Comet	$B-V$	$V-R$	$R-I$	SSA	b	$\bar{\theta}$	A_{geo}	$\beta[mag/^\circ]$	phase angle coverage
67/P CG[a]	0.73 ± 0.07	0.57 ± 0.03	0.59 ± 0.04	0.052 ± 0.013	-0.42	$19^{\circ}{}^{+4}_{-9}$	0.062 ± 0.002	0.077 ± 0.002[b] , 0.041 ± 0.001[c]	$1.2^\circ - 111.5^\circ$
67/P CG[d]	-	-	-	0.037 ± 0.002	-0.42 ± 0.03	15°	0.059 ± 0.02[e]	0.047 ± 0.002	$1.3^\circ - 53.9^\circ$
67/P CG[f]	-	0.52 ± 0.05	-	-	-	-	-	-	4.8°
67/P CG[g]	0.83 ± 0.08	0.54 ± 0.05	0.46 ± 0.04	-	-	-	-	$0.061 - 0.076$	$0.5^\circ - 10.6^\circ$
1P/ Halley[h]	0.72 ± 0.04	0.41 ± 0.03	0.39 ± 0.06	-	-	-	-	-	107°
19P/ Borrelly[i]	-	-	-	0.057 ± 0.009	-0.43 ± 0.07	$22^\circ \pm 5^\circ$	0.072 ± 0.020	0.043	$51^\circ - 75^\circ$
19P/ Borrelly[l]	-	0.25 ± 0.78	-	-	-	-	-	-	??
103P/ Hartley 2[m]	0.75 ± 0.05	0.43 ± 0.04	-	0.036 ± 0.006	-0.46 ± 0.06	$15^\circ \pm 10^\circ$	0.045 ± 0.009	0.046 ± 0.002	$79^\circ - 93^\circ$
9P/ Tempel1[n]	0.84 ± 0.01	0.50 ± 0.01	0.49 ± 0.02	0.039 ± 0.005	-0.49 ± 0.02	$16^\circ \pm 8^\circ$	0.051 ± 0.009	0.046 ± 0.007	$63^\circ - 117^\circ$
81/P Wild 2[o]	-	-	-	0.038 ± 0.04	-0.52 ± 0.04	$27 \pm 5^\circ$	0.059	0.0513 ± 0.0002	$11^\circ - 100^\circ$

Notes. [a] **This work**
[b] **for** $\alpha < 15^\circ$
[c] **for** $\alpha > 15^\circ$
[d] w, b **(at 0.535** μm**),** $\bar{\theta}$ **and** β **from Fornasier & et al. (2015)**
[e] **Sierks et al. (2015)**
[f] **Lamy et al. (2006)**
[g] **Tubiana et al. (2011).** $B-V$ **has been computed from** $B-R$ **and** $V-R$ **measurements reported in Tubiana et al. (2011)**
[h] **Thomas & Keller (1989)**
[i] **photometric parameters derived in R band by Li et al. (2007b) . Ground based observations with solar phase angle down to** 13° **have been included to compute the slope parameter.**
[l] **Lowry & Weissman (2003)**
[m] **Li et al. (2013) .***Gemini* **and** HST **observations at low phase angle have been included to constrain Hapke modeling and derive the slope parameter.**
[n] **photometric parameters derived in R band Li et al. (2007a) . Ground based and** HST **observations with solar phase angle down to** 4° **have been included to compute the slope parameter.**
[o] **photometric parameters derived in R band by Li et al. (2009)**

6. Conclusions and future work

We have studied the photometric properties of the comet 67/P Churyumov-Gerasimenko as observed by the VIRTIS-M instrument onboard the Rosetta mission. The investigation has been developed in two parts, one concerning the analysis of full-disk observations of the comet and one based on disk-resolved images. In the case of full-disk observations we computed the integrated flux from the nucleus in order to derive the light curve of CG at different phase angles. The light curve, as measured by VIRTIS, shows a double-peak behavior, due to the elongated shape of the nucleus and is in good agreement with the one derived by Mottola et al. (2014). Since full-disk observations have been taken at low phase angles we also gave a preliminary characterization of the OE surge, suggesting Shadow Hiding as the driving mechanism.

Color ratios in the VIS and IR ranges have been calculated in order to exploit large scale compositional differences on the surface, with negative results. Taking advantage of full disk data at very low phase ($\alpha < 1^\circ - 2.5^\circ$) we gave an estimate of the normal albedo at 0.55 μm obtaining $A_n = 0.062 \pm 0.002$. This value has been assumed to match the geometric albedo A_{geo}, following the considerations of sec. 2.4.

Moving to disk-resolved images, we used the huge dataset produced by VIRTIS-M so far to derive a photometric reduction to single scattering albedo and simultaneously determine the photometric properties of the nucleus. The photometric reduction we applied is a simplified Hapke model, where OE effect and multiple scattering have been neglected, since our phase angle coverage is limited to the range $27.2^\circ < \alpha < 111.5^\circ$ and CG surface is very dark. We retrieve a backscattering single particle phase function ($b = -0.42$ at 0.55 μm) and single scattering albedo $w = 0.052 \pm 0.013$. Surface roughness is determined by the average slope parameter $19^{\circ\,+4}_{-9}$.

We also investigated the phase reddening effect. Our conclusion on this topic is that it is mainly due to single scattering, through a wavelength-dependent phase function, and the role of multiple scattering can be neglected. We measure a phase reddening of $0.44\%/^\circ$ in the VIS, while, for comparison, no reddening has been observed on Tempel 1 (Li et al. 2007a). Color indices in the VIS range indicate that CG spectral properties are typical in the context of cometary nuclei, except for $R - I$, which is larger than the average and indicating an increase of the reddening longward in the VIS.

Albedo maps have been produced by means of photometrically reduced data. It emerges that the "neck" (Hapi region) and the center of the "bottom" (Imothep plain) are sligthly brighter than the rest of the nucleus. The former shows a more neutral spectrum while the second appears redder, similarly to the rest of the surface ("head" and "body").

A future development of this work will concern the inclusion of the OE in the modeling, taking advantage of the more recent disk-resolved acquisitions at low phase angles. We will also compare the photometric properties of the nucleus before and after the perihelion passage (13 August 2015), in order to exploit the modification of the photometric parameters induced by the cometary activity

485 to better constrain the composition and textural properties of the surface materials as well as their
486 changes with time.

487 References

488 Akimov, L. A. 1988, Kinematika i Fizika Nebesnykh Tel, 4, 3
489 Bessell, M. S. 1986, Astronomical Society of the Pacific, Publications, 98, 1303
490 Bessell, M. S. 1990, Astronomical Society of the Pacific, Publications, 102, 1181
491 Buratti, B. J., Hicks, M. D., Soderblom, L. A., et al. 2004, Icarus, 167, 16
492 Capaccioni, F., Coradini, A., Filacchione, G., et al. 2015, Science, 347, 628
493 Ciarniello, M., Capaccioni, F., & Filacchione, G. 2014, Icarus, 237, 293
494 Ciarniello, M., Capaccioni, F., Filacchione, G., et al. 2011, Icarus, 214, 541
495 Clark, B. E., Helfenstein, P., Bell, J. F., et al. 2002, Icarus, 155, 189
496 Coradini, A., Capaccioni, F., Drossart, P., et al. 2007, Space Sci. Rev., 128, 529
497 Cuzzi, J. N., French, R. G., & Dones, L. 2002, Icarus, 158, 199
498 Domingue, D. L., Lockwood, G., & Thompson, D. 1995, Icarus, 115, 228
499 Filacchione, G., Capaccioni, F., Ciarniello, M., et al. 2012, Icarus, 220, 1064
500 Filacchione, G., Ciarniello, M., Capaccioni, F., et al. 2014, Icarus, 241, 45
501 Fornasier, S. & et al. 2015, Astron. Astrophys., This issue
502 Hapke, B. 1993, Theory of reflectance and emittance spectroscopy, Topics in Remote Sensing, 3 (Cambridge, UK: Cam-
503 bridge University Press)
504 Hapke, B. 2002, Icarus, 157, 523
505 Hapke, B. 2008, Icarus, 195, 918
506 Hapke, B. 2012, Theory of reflectance and emittance spectroscopy (Cambridge University Press)
507 Hapke, B., Nelson, R., & Smythe, W. 1998, Icarus, 133, 89
508 Heyney, L. G. & Greenstein, J. L. 1941, Astrophys. J., 93, 70
509 Kaydash, V., Pieters, C., Shkuratov, Y., & Korokhin, V. 2013, Journal of Geophysical Research (Planets), 118, 1221
510 Keller, H. U., Barbieri, C., Lamy, P., et al. 2007, Space Sci. Rev., 128, 433
511 Lagerkvist, C.-I. & Magnusson, P. 1990, Astron. Astrophys., 86, 119
512 Lamy, P. L., Toth, I., Weaver, H. A., et al. 2006, Astron. Astrophys., 458, 669
513 Li, J.-Y., A'Hearn, M. F., Belton, M. J. S., et al. 2007a, Icarus, 187, 41
514 Li, J.-Y., A'Hearn, M. F., Farnham, T. L., & McFadden, L. A. 2009, Icarus, 204, 209
515 Li, J.-Y., A'Hearn, M. F., McFadden, L. A., & Belton, M. J. S. 2007b, Icarus, 188, 195
516 Li, J.-Y., Besse, S., A'Hearn, M. F., et al. 2013, Icarus, 222, 559
517 Li, J.-Y., Helfenstein, P., Buratti, B. J., Takir, D., & Clark, B. E. 2015, ArXiv e-prints [arXiv:1502.06302]
518 Longobardo, A., Palomba, E., Capaccioni, F., et al. 2014, Icarus, 240, 20
519 Lowry, S. C. & Weissman, P. R. 2003, Icarus, 164, 492
520 Minnaert, M. 1941, Astrophys. J., 93, 403
521 Mottola, S., Lowry, S., Snodgrass, C., et al. 2014, Astron. Astrophys., 569, L2
522 Preusked, F., Scholten, F., & Knollenberg, J. 2015, Planetary and Space Science
523 Raponi, A. 2015, ArXiv e-prints [arXiv:1503.08172]
524 Schröder, S. E., Grynko, Y., Pommerol, A., et al. 2014, Icarus, 239, 201
525 Shepard, M. K. & Helfenstein, P. 2011, Icarus, 215, 526
526 Shkuratov, Y., Kreslavsky, M. A., Ovcharenko, A. A., et al. 1999, Icarus, 141, 132
527 Sierks, H., Barbieri, C., Lamy, P. L., et al. 2015, Science, 347, 1044
528 Snodgrass, C., Fitzsimmons, A., Lowry, S. C., & Weissman, P. 2011, Monthly Notices of the Royal Astronomical Society,
529 414, 458
530 Thomas, N. & Keller, H. U. 1989, Astron. Astrophys., 213, 487

Thomas, N., Sierks, H., Barbieri, C., et al. 2015, Science, 347, 440

Tubiana, C., Böhnhardt, H., Agarwal, J., et al. 2011, Astron. Astrophys., 527, A113

[1] IAPS-INAF, via Fosso del Cavaliere, 100, 00133, Rome, Italy

[2] Laboratoire d'Etudes Spatiales et d'Instrumentation en Astrophysique, Observatoire de Paris/CNRS/Université Pierre et Marie Curie/Université Paris-Diderot, Meudon, France

[3] Institute of Planetary Research, DLR, Berlin, Germany

[4] Laboratoire de Planétologie de Grenoble (LPG) - University Joseph Fourier Grenoble, Grenoble, France

List of Objects